Design and Experimental Validation of a Semi-Passive Shoulder Exoskeleton
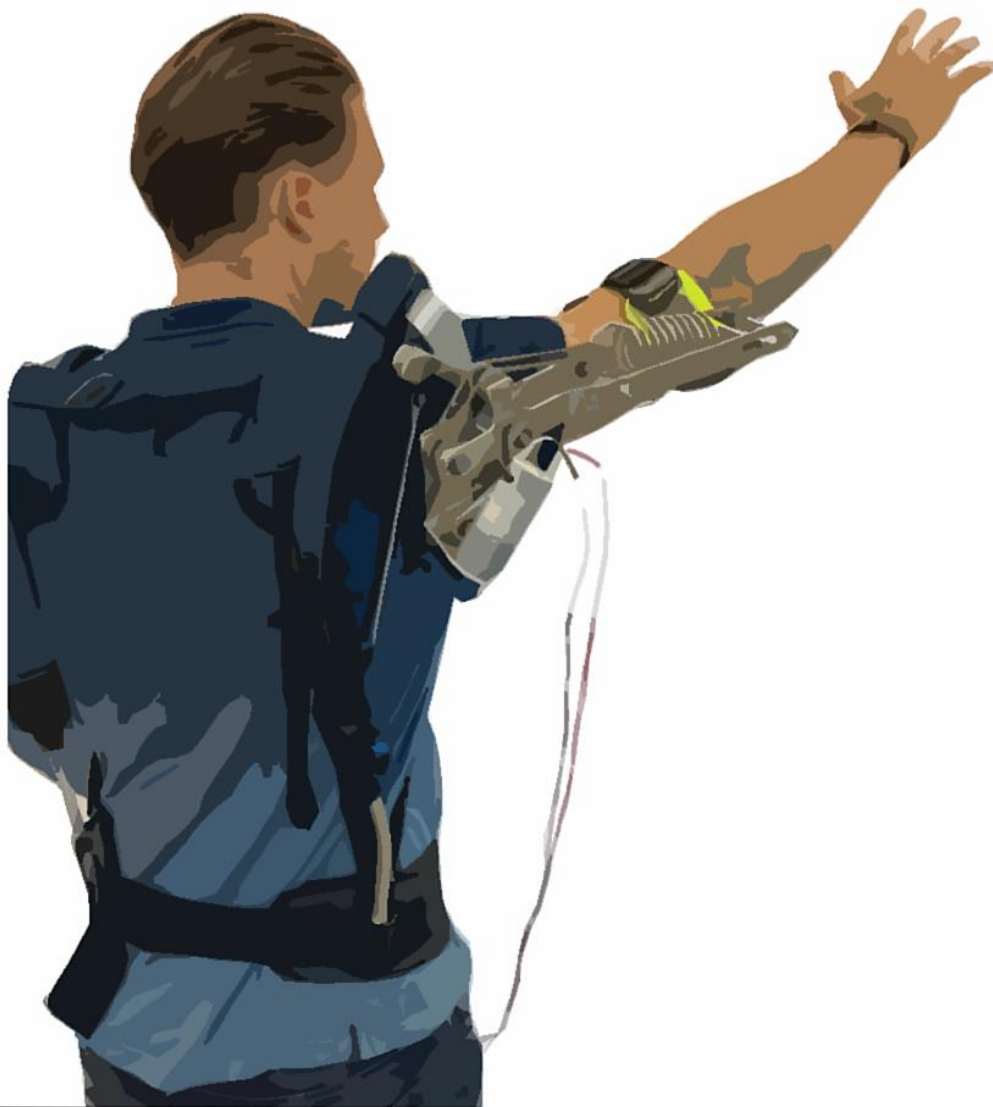
S.L.C. Schuurbiers

TUDelft

skelex

Design and Experimental Validation of a Semi-Passive Shoulder Exoskeleton

Improvement of Load Reduction Performance of the Passive Skelex 360-XFR Shoulder Exoskeleton

by

Stefan Schuurbiers

to obtain the degree of Master of Science
at the Delft University of Technology,
to be defended publicly on November 18, 2022, at 14:30.

Student number:	4586948	
Project duration:	March 1, 2022 – November 18, 2022	
Thesis committee:	Dr. ir. W. Mugge,	TU Delft, supervisor
	Prof. dr. ir. P. Breedveld,	TU Delft
	Ir. G. Genani,	Skelex B.V.

This thesis is confidential and cannot be made public until December 31, 2024.

An electronic version of this thesis is available at http://repository.tudelft.nl/.

TUDelft

CONTENTS

Design and Experimental Validation of a Semi-Passive Shoulder Exoskeleton

Stefan Schuurbiers, Winfred Mugge, and Gaurav Genani

Abstract—Of all reported cases, muscular pain in the arms is the second main cause of work-related musculoskeletal disorders (WMSDs) in European workers. The most popular prevention method for shoulder-related WMSDs are passive shoulder exoskeletons, as of their light weight and ease of use. Yet, due to their static force-angle characteristic, passive shoulder exoskeletons show a limited load reduction effect for dynamic tasks. Active shoulder exoskeletons show better performance in the reduction of loads for dynamic tasks, but are not accepted in industrial environments due to their high weight and complexity. In this study, the advantages of both passive and active shoulder exoskeletons have been combined in the design of a mechanism that can actively alter the force-angle characteristic of the Skelex 360-XFR passive shoulder exoskeleton, increasing its load reduction performance, and hence making it a more effective prevention method to WMSDs. By experiments using a prototype, it has been shown that a drivable parallelogram linkage capable of inducing angular changes between an in-going lever arm link and an out-going link to the user's arm, can effectively induce proportional phase changes of the conventional force-angle characteristic, and that the model predicting the optimal stiffness of the spring used in the implemented force-balancing mechanism is reliable. With the experimental findings, recommendations have been made regarding the minimum capacity in output torque of the actuator, 0.38 Nm, and the stiffness of the balancing spring, 1752 N/m, to end up with optimal weight, size, and power consumption of the semi-passive shoulder exoskeleton.

Index Terms—Semi-Passive Exoskeleton, Work-Related Musculoskeletal Disorders, Industry, Shoulder, Hybrid.

✦

1 INTRODUCTION

1.1 Background

Work-related musculoskeletal disorders (WMSDs) are one of the main reported health problems in occupational environments in Europe [9]. Of all the reported cases, muscular pain in the arms is the second main cause of sick-leave in European workers (43%) [8]. WMSDs related to the upper limb are most commonly developed in workers that practice jobs that require repetitive and excessive motions of the upper body [21]. Since recovery of WMSDs often requires workers to stay home for a significant period of time, financial burdens arise for the employers and society [5].

To prevent WMSDs, one could argue that high-risk jobs should be automated. However, as most of these high-risk jobs involve dynamic tasks that require human-level capacities such as perception, dexterity, and adaptability, automation is not an option [8], [21]. A solution that could both prevent WMSDs and preserve the quality of the conducted tasks are exoskeletons. Exoskeletons are wearable devices that can reduce the load on workers, and in some cases enhance human strength. As indicated by Missiroli et al. [16], recent studies have proven the effectiveness of exoskeletons in the reduction of biomechanical loads across a large variety of work environments and manual tasks. In general, a distinction can be made between three types of exoskeletons: passive, active, and semi-passive exoskeletons.

Most of the exoskeletons currently used in industrial environments are of passive nature. Examples of commercially available passive shoulder exoskele-tons are [9]: the MATE Exoskeleton developed by Comau, the ShoulderX V3 developed by SuitX, the Paexo Shoulder developed by Ottobock, the Ekso vest developed by Ekso Bionics, the EXHAUSS system developed by EXHAUSS, the BESK G exoskeleton developed by GOGOA, and the Skelex 360-XFR by Skelex [18]. These are generally spring-based devices that provide the worker with a specific "static" force-angle related support, of which its main purpose is to compensate for the biomechanical loads induced by the weight of the upper limb itself. Apart from the proven effectiveness of passive exoskeletons on the reduction of biomechanical loads in the shoulder, a shortcoming of these devices is that none can accommodate task-related variations in the force-angle behaviour of the support force. This poses an issue, because many strenuous or labor-intensive tasks are of variable nature and hence not effectively compensated by one static support force profile [21].

Several studies exist in which active shoulder exoskeletons are designed and evaluated [15]. The advantage of active exoskeletons is that a task-specific support could be provided to a user. Moreover, besides compensating the weight of the upper limb, active exoskeletons have the potential to compensate for external loads such as tools as well. Although active exoskeletons show a great potential as a prevention method to WMSDs, only few active shoulder exoskeletons are commercially available. Reasons for that are the low acceptance of active exoskeletons in the industry because of their bulkiness, high weight,

and complexity [8], [15].

A solution that combines both the high adaptability of active shoulder exoskeletons and the wide usability of passive shoulder exoskeletons is referred to as semi-passive exoskeletons. Semi-passive exoskeletons make use of low-power actuation units to modulate the behaviour of the spring-based actuation mechanisms and hence provide an extra degree of adaptivity compared to passive exoskeletons [8], [11].

1.2 State-of-the-Art

1.2.1 Skelex 360-XFR Shoulder Exoskeleton

This study is commissioned by Skelex B.V. that produces a commercially available passive shoulder exoskeleton called the Skelex 360-XFR. The goal of this exoskeleton is to reduce loads in the shoulder joint for overhead tasks, and hence to reduce the risk on WMSDs. In Figure 1, a schematic representation of the Skelex 360-XFR has been presented.
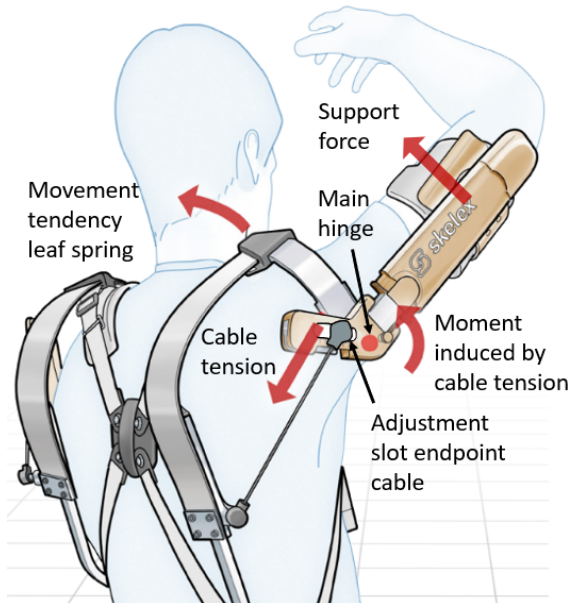

Figure 1: Schematic representation of the Skelex 360-XFR, with its main working principle indicated by red arrows. Deflection of the leaf spring causes tension in the cable. Since the cable has a distance, specified by the adjustment slot, to the main hinge, a counterclockwise moment is induced. As the user's arm is placed in the arm cup at the end of the L-shaped mechanism, the moment around the main hinge results in a support force on the arms.

The Skelex 360-XFR is constructed of a leaf spring, a rotatable L-shaped link, and a cable. A support force is induced on the user's arm by the release of potential energy of the leaf spring. If a user moves his/her arms completely down, the leaf spring will be deflected maximally. Deflection is induced because the endpoint of the cable is forced to rotate with the same path as the L-shaped link. Since the length of the cable is constant, a clockwise rotation of the L-shaped mechanism forces the leaf spring to deflect.

Deflection of the leaf spring inherently results in an increase in cable tension and hence an increase in clockwise moment around the main hinge. Normally, that moment would result in a rotation of the L-shaped link to a static equilibrium, but the presence of the user's arm in the arm cup connected to the L-shaped link results in a support force counteracting it.

The support force of the Skelex 360-XFR follows a typical force-angle related characteristic, as depicted by the dashed sine shaped profile in Figure 2b. By adjusting the endpoint of the cable within the slot, the amplitude of this characteristic can be adjusted, whereas the shape remains the same. That is, because only the magnitude of the effective lever arm is adjusted and not its function dependent on the rotation of the L-shaped link. Due to its force-angle characteristic, the Skelex 360-XFR is mostly used in jobs that require the worker to frequently conduct overhead tasks. Examples of typical use-cases are plasterers, welders and assemblers in a car factory.

1.2.2 Limitations Skelex 360-XFR Shoulder Exoskeleton

An important requirement of a shoulder exoskeleton is that it must bring loads in the shoulder joint to a minimum. However, most of the commercially available passive exoskeletons have a fixed force-angle related support characteristic that only compensates the gravitational loads in the shoulder induced by the arm's own mass. The same holds true for the Skelex 360-XFR, meaning that its effectiveness in the reduction of loads in the shoulder (biomechanical effectiveness) is limited for dynamic tasks.

To gain an understanding of the biomechanical effectiveness of the Skelex 360-XFR for dynamic tasks, an analysis of resultant loads in the shoulder of a user has been made for a pick-and-place task of a box with a known mass (see Figure 2(a)). Utilizing the tracked positions of the upper limb's joints (shoulder, elbow, and wrist) and making use of body segment parameters as discussed by de Leva et al. [13], the support force required to minimize the loads in the shoulder during the task has been calculated.

As observable from Figure 2(b), in a relatively large part of the movement, the Skelex 360-XFR, is not able to provide the user with the 'ideal' support force required to minimize the biomechanical loads in the shoulder. The main reason for that is the fixed sinusoidal shaped force-angle characteristic, as presented by the dashed lines in Figure 2(b). Even in regions where the exoskeleton could potentially provide a sufficient amount of support that would minimize the loads in the shoulder, the actual provided support is generally too high. Hence, a more effective solution would be an exoskeleton that could, independent of its configuration, provide the user with any required force within a specific magnitude range. That range would be determined by the maximum force the exoskeleton could provide without breaking (repre-
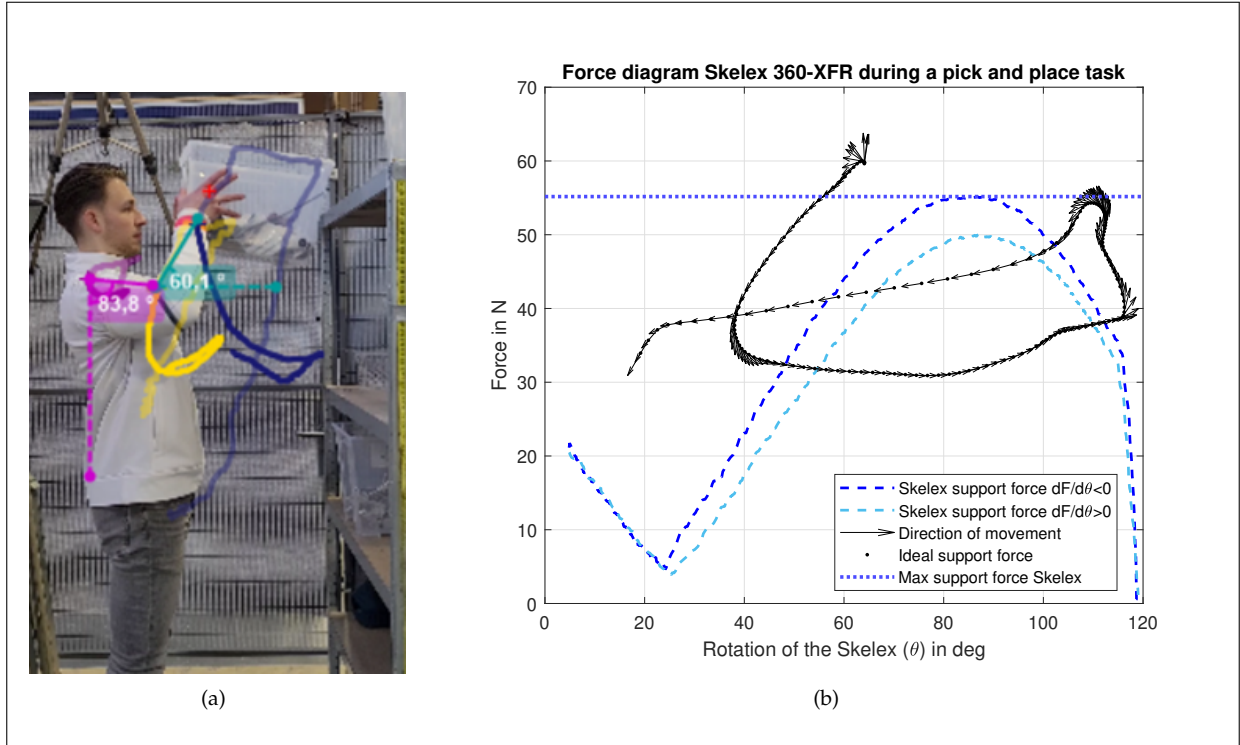
Figure 2: Analysis of the biomechanical effectiveness of the conventional passive Skelex 360-XFR exoskeleton. **(a)** Pick-and-place task of a box of known weight. In total, 3 nodes are tracked using the Kinovea software: one placed on the shoulder as tracked in purple, one placed on the elbow as tracked in yellow, and one placed on the wrist as tracked in blue. The relative positions are stored and analyzed in MATLAB. **(b)** Analysis of the task data as obtained by the video tracking software, Kinovea. As a reference, the force-angle curve (dashed lines) of the Skelex 360-XFR has been presented. It is observable that this force-angle curve contains a hysteresis loop. In black, the ideal required support force has been indicated that would minimize the biomechanical loads in the shoulder joint. The movement direction has been indicated by black arrows. The dotted line presents the maximum force the exoskeleton could provide.

sented by the dotted line in Figure 2b).

Since each task requires a different support force profile of the exoskeleton to minimize the loads in the shoulder, a conversion from a passive into a semi-passive exoskeleton would be an interesting solution to increase its biomechanical effectiveness. In this way, low power actuation can actively adjust the magnitude of the support force such that resultant loads in the shoulder joint are most effectively minimized for any position of the arms within the range of motion (ROM) of the exoskeleton.

1.2.3 Semi-Passive Mechanisms in Exoskeletons

Several semi-passive mechanisms in exoskeletons are presented in literature that can actively alter the behaviour of the support force experienced by the user. In the H-PULSE exoskeleton [8] a method is used where the pretension of the passive energy source can be actively altered by means of an actuated sliding mechanism. Yet, only the magnitude of the characteristic force-angle curve can be adjusted and not its effective location in terms of the arm's position, minimizing the increase in load reduction performance in comparison to its passive counterpart. The AGADE semi-passive exoskeleton [1] is based on a slightly different principle that is formed by a parallelogram linkage. By actuating the endpoint of the spring within

this linkage, both its pretension and effective stiffness component can be altered such that a task-specific support force can be provided to the user. A semi-passive mechanism that has been implemented in a leg exoskeleton is called the MACCEPA [3]. This mechanism is capable of actively changing the stiffness of a joint by actuation of a lever arm and the pretension of a spring at the same time. Hence, a wide range of force profiles can be provided to the user.

Since the discussed state-of-the-art semi-passive mechanisms are patented and/or specifically designed for one exoskeleton, they cannot be directly implemented in other commercial passive exoskeletons as a method to increase their load reduction performance. Hence, a custom solution needs to be devised for when the load reduction performances of an existing passive exoskeleton need to be increased.

1.3 Problem Definition & Goal

The passive shoulder exoskeleton, Skelex 360-XFR, has shown to be effective in load reduction in the shoulder for static overhead tasks, but lacks in effectiveness when tasks become dynamic and external loads come in play. Since most jobs involve dynamic tasks with tools, and thus external loads on the arms, the Skelex 360-XFR will not be a sufficient prevention method for WMSDs. Semi-passive exoskeletons have shown

to be more effective for dynamic tasks, but involve exoskeleton-specific and patented mechanisms, making them unsuitable to implement in the Skelex 360-XFR directly. That is why the goal of this study is to develop a mechanism that increases the load reduction performance of the Skelex 360-XFR for dynamic tasks, making it a more effective prevention method to WMSDs.

1.4 Lay-out

The structure of this study is as follows: essential requirements are established in Section 2 after which the generated concepts are presented in Subsection 3.1. One concept was selected, regarded as most promising, based on a grading method as presented in Subsection 3.2. The selected concept was further developed and optimized based on a theoretical background as discussed in Subsection 3.3. With the design parameters established from the model, a prototype was designed as presented in Subsection 3.4. This prototype was used to conduct experiments with, of which the structure and design are explained in Subsection 4.1. The results from these experiments are presented in Subsection 4.2 and evaluated in Section 5. In the end, a conclusion is drawn regarding the conversion of the Skelex 360-XFR into a semi-passive exoskeleton, as presented in Section 6.

2 DESIGN REQUIREMENTS

2.1 Overview

For the construction of the design requirements, a distinction has been made between two categories:

- Functional requirements, that describe what the design must do in order to be functional.
- Constraints, that define the design space and restrictions on the mechanism.

Both the functional requirements and the constraints are black/white, meaning that if a design does not meet these requirements, it is per definition not regarded as a solution.

2.2 Functional Requirements

- It must be possible to actively adjust the support force of the exoskeleton during usage.
- It must be possible to provide the user with any magnitude of support force up to the maximum support force, for any angle within the ROM of the exoskeleton (0 to 120 degrees with respect to arms hanging vertically down).
- It must be possible to have a support force smaller than 10 N, at least in the region between 0 and 45 degrees (arms hanging vertically down and arms flexed to a 45 degree position, respectively). This allows the user to have a resting position for the arms.

2.3 Constraints

- The passive energy source of the Skelex 360-XFR, i.e. the leaf spring, cannot be replaced.
- The leaf spring of the exoskeleton cannot be over-deflected (maximum deflection in y-direction $(du_{y,max}) \approx 110$ mm, and maximum deflection in x-direction $(du_{x,max}) \approx 110$ mm, as derived from a video tracking experiment of the leaf spring in Kinovea (see Appendix B)). Over-deflection can lead to delamination of the leaf spring and, thus, failure of the exoskeleton.
- The weight of the exoskeleton cannot exceed 5 kg. This has been established after a discussion with a representative of a number of users in a car assembly factory.
- The exoskeleton cannot protrude more than 150 mm from the body in any direction. If a mechanism exceeds this constraint, it is expected to negatively affect user acceptance.

3 DESIGN STRATEGY

3.1 Concept Generation

3.1.1 Overview

Based on the design requirements, four concepts have been generated. The main goal of each concept was to increase the providable range of support forces compared to the Skelex 360-XFR, whilst still using the same leaf spring, by converting it into a semi-passive suit capable of providing active force adjustment. For each concept, an explanation of the working principle will be provided that declares how that goal could be achieved.

3.1.2 Concept I: Parallelogram Linkage

One way of converting the Skelex 360-XFR into a more versatile and biomechanical effective suit, is by implementing a mechanism capable of inducing phase changes in its conventional force-angle characteristic, such that the maximum of this curve could be present at any angle within the ROM of the exoskeleton. The only limiting factor in the amount of support a user could get would then be the maximum providable force by the leaf spring without yielding.

Phase changes in the force-angle characteristic of the Skelex 360-XFR can be induced by changing the angle between the in- and out-going link of the L-shaped part of the conventional Skelex 360-XFR. A simplified presentation of the Skelex 360-XFR's working principle is made in Figure 3a. As the moment induced by the spring force F_{spring} is independent of the configuration of the out-going link that transmits the support force to the user's arm, it should be possible to alter the angle between the lever arm link (I-R) and the arm link (R-O) such that a phase difference between the two situations is present as depicted in Figure 3b.

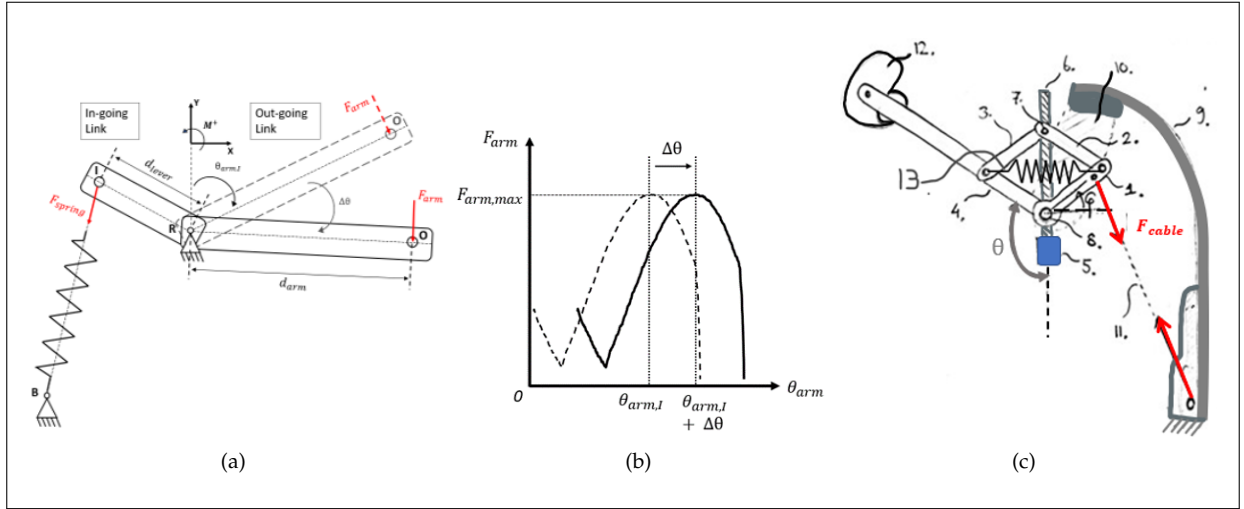Since we are working towards the design of a

Figure 3: **(a)** Simplified schematic representation of the Skelex 360-XFR to prove the phase change principle. The force exerted by the leaf spring (or the cable) in the actual suit is represented by a tension spring connected to a base B. The spring force F_{spring} is exerted on a lever arm at point I with its length defined by d_{lever}. The length of the arm link through which the moment is converted into a support force at point O is defined by d_{arm}. The main hinge is referred to as R, around which the entire L-shaped mechanism can rotate. In principle, both the lever arm (in-going link) and the arm link (out-going link) act as one rigid body, but the relative angle can be changed as determined by $\Delta\theta$. The configuration of the out-going link is thus determined by $\theta_{arm} + \Delta\theta$, with the phase determined by the change in relative angle $\Delta\theta$. **(b)** This plot shows the phase shift between the different positions as presented by the two outgoing links in image (a). The dashed curve belongs to the out-going represented by the dashed line, and the solid curve belongs to the out-going link represented by the solid line. **(c)** Drawing of Concept I, in which: 1. the lever arm link, 2. and 3. are coupler links, 4. the arm link, 5. the actuator, 6. the lead screw, 7. the position of the lead screw nut, 8. the main hinge, 9. the leaf spring, 10. the shoulder piece and functions as a base, 11. the steel cable, 12. the arm cup, and 13. a balancing spring.

semi-passive suit, it is essential that the mechanism capable of inducing phase changes of the force-angle characteristic can be actuated by means of a low-power actuation unit. Mounting a motor directly on the lever arm link and using the arm link as an outgoing link would be a simple solution, however this will require a high torque output from the actuator, thereby resulting in a large and heavy motor. The performance of the exoskeleton will be negatively influenced by that. Hence, a more refined solution is preferred that requires a minimum power output of the actuator. One way to achieve such a solution is by means of a parallelogram linkage, as presented in Figure 3c. Essentially, this parallelogram linkage has the same working principle as the conceptual L-shaped mechanism presented in Figure 3a with an additional feature being the possibility of actively inducing phase changes of the force-angle characteristic.

As discussed, a change in angle between the lever arm link (1.) and the arm link (4.), as presented in Figure 3c, will result in a phase shift of the force-angle curve of the exoskeleton. That angle can be controlled by means of an actuation mechanism comprising a motor (5.) and a lead screw (6.), capable of changing the height of node (7.). Since a parallelogram linkage has been formed by members (1.-4.), a change in this height will inherently result in a change in the angle between links (1.) and (4.), and thus also in a phase change of the force-angle characteristic of the exoskeleton. When the height of node (7.) has been set, the linkage mechanism acts as one rigid body that rotates around the main hinge (8.) mounted at a base

(10.), just as the L-shaped link in the Skelex 360-XFR. Hence, the shape of the force-angle curve will not be affected by this actuation, only its phase will be changed. If the lever arm (1.) is rotated anti-clockwise whilst the arm link (4.) keeps its configuration, the leaf spring (9.) will bend and the tension in the cable (11.), referred to as F_{cable}, will increase. This force tends to 'collapse' the parallelogram linkage, and thus pushes node (7.) downward on the lead screw (6.), resulting in high friction forces for high deflections of the leaf spring. High friction forces on the lead screw results in a high required torque output of the motor, which is undesired, since this will lead to a large shaped motor with a large weight. As a solution, a spring (13.) is used to counteract the 'collapsing' behaviour by pushing node (7.) upward. Clever selection of the spring characteristics could bring the maximum required output torque from the motor to a minimum, which inherently means that the motor's weight and size are minimized.

3.1.3 Concept II: 2-Drive Linkage

Instead of only being capable of inducing phase shifts, this concept can also induce magnitude changes in the force-angle characteristic of the conventional Skelex 360-XFR. The purpose of this additional feature is to potentially simplify control in later stages and to decrease the adjustment time. The magnitude of the force-angle characteristic can be altered by changing the lever arm length, as presented by d_{lever} in Figure 4a. It is known from the passive exoskeleton that a reduction in lever arm results in a lower amplitude
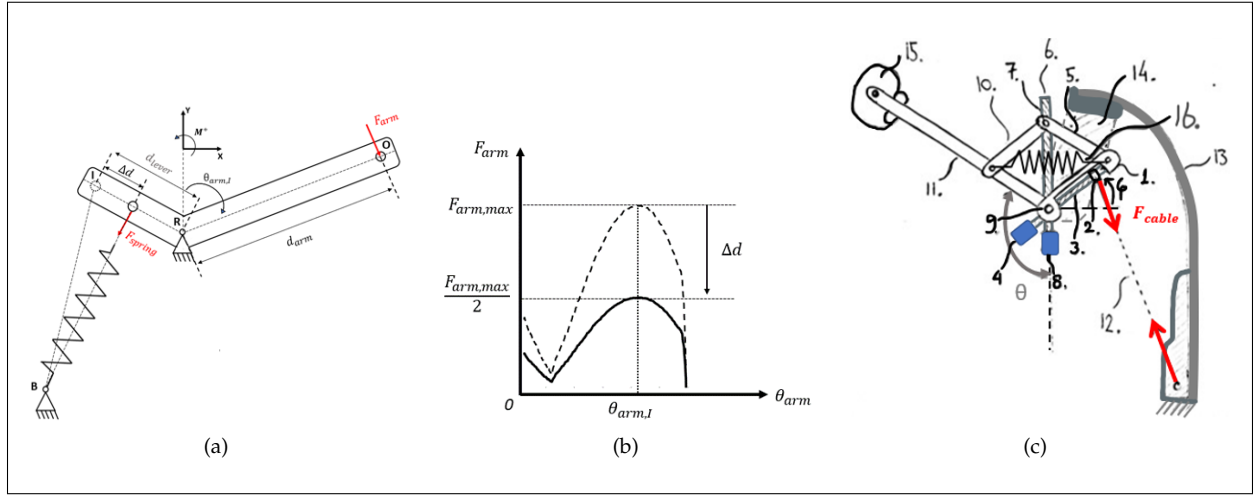
Figure 4: Effects resulting from a change in lever arm length, as defined by Δd. **(a)** Changing the lever arm length by a magnitude of Δd will result in a magnitude change between the force-angle curves between the two situations. **(b)** Here the change in force-angle curve has been presented for a situation when the lever arm length is halved, so $\Delta d = \frac{d_{lever}}{2}$. As observable, the magnitude of the force curve is being halved as well. **(c)** Drawing of Concept II, in which: 1. the lever arm link, 2. the lead screw nut of the lever arm, 3. the lead screw at the lever arm, 4. the actuator of the lever arm, 5. & 10. the coupler links, 6. the lead screw in the parallelogram linkage, 7. the position of the lead screw nut of the parallelogram linkage, 8. the actuator of the parallelogram linkage, 9. the main hinge, 11. the arm link, 12. the steel cable, 13. the leaf spring, 14. the shoulder piece, 15. the arm cup, 16. the balancing spring.

of the force-angle curve, as depicted in Figure 4b. Combining this behaviour with the phase changes that occur when the angle between the lever arm link and the arm link is adjusted (see Figure 3b), could result in a simpler and faster actuation method in comparison to Concept I.

A control method that could be interesting to implement is to change the phase of the force-angle curve in such a manner that the angle of the lever arm (indicated by ϕ in Figure 4c) remains constant. By doing that, maximum force can be present at every angle of the arm link (11.) as defined by F$_{arm,max}$ in Figure 4b. In order to vary the magnitude of the support force exerted on the user's arm by the arm cup (15.) (see Figure 4c), the length of the lever arm should be changed. A second actuator (4.) connected to a lead screw (3.) can vary the position of a lead screw nut (2.) at which the cable force F_{cable} is acting. Hence, the length of the lever arm can be varied actively. Besides the additional actuation mechanism for the lever arm length, the working principle has remained similar compared to Concept I.

3.1.4 Concept III: CAM Link

Concepts I and II are based on mechanisms that can shift the characteristic force-angle curve of the passive exoskeleton such that, regardless the angle of the arms, a range of forces can be provided as determined by the maximum deflection of the leaf spring. Another way to provide the user with a range of forces independent of the position of the arms is a mechanism that exerts a constant force on the user's arm. If one would be able to reach a constant force-angle characteristic with a similar magnitude to the maximum force of the Skelex 360-XFR, an additional mechanism could be designed capable of altering the magnitude of the constant force.

As a result, a region is formed in which any support force could be provided to the user between 0 N and the maximum support force $F_{arm,max}$ (Figure 5(b)).

The concept presented here provides a constant force to the user's arm, by making use of a variable radius wheel (CAM) at the beginning of the arm link (see Figure 5(a)). Usually a CAM transfers a rotary motion into a linear motion, but in this case the shape of the CAM is designed so that it accounts for the increase in spring force when the arm link is rotated. The radius of the CAM must be proportional to the increase in spring force to preserve a constant moment around the main hinge R, and thus a constant force (F_{arm}) provided to the user's arm. As it is not always required to have one specific magnitude of force at all angles of the arm link (θ_{arm}), a mechanism has been implemented that could change the pretension of the spring, having a direct effect on the constant force exerted on the user's arm. As an example (see Figure 5a-b), the maximum pretension of the spring, resulting in the maximum support force $F_{arm,max}$, is decreased from $u_{i,max}$ to $u_{i,2}$. As a result, a lower support force ($F_{arm,2}$) will be present at the arm. In principle, this can be done for the whole range of pretensions that are lower than $u_{i,max}$, such that any constant force lower than $F_{arm,max}$ can be provided.

In Figure 5c the concept has been schematically depicted as if it is attached to the frame of the Skelex 360-XFR. The CAM (1.) that is part of the arm link (3.) and rotates about the main hinge (2.) will result in a constant force transmission at the arm cup (11.) when the leaf spring (9.) is deflected. Deflection of the leaf spring occurs when the arm link, and thus the CAM, rotates around the main hinge and thereby wounds the cable (6.) over its circumference. As it is not always desired to have one specific amount of constant force,
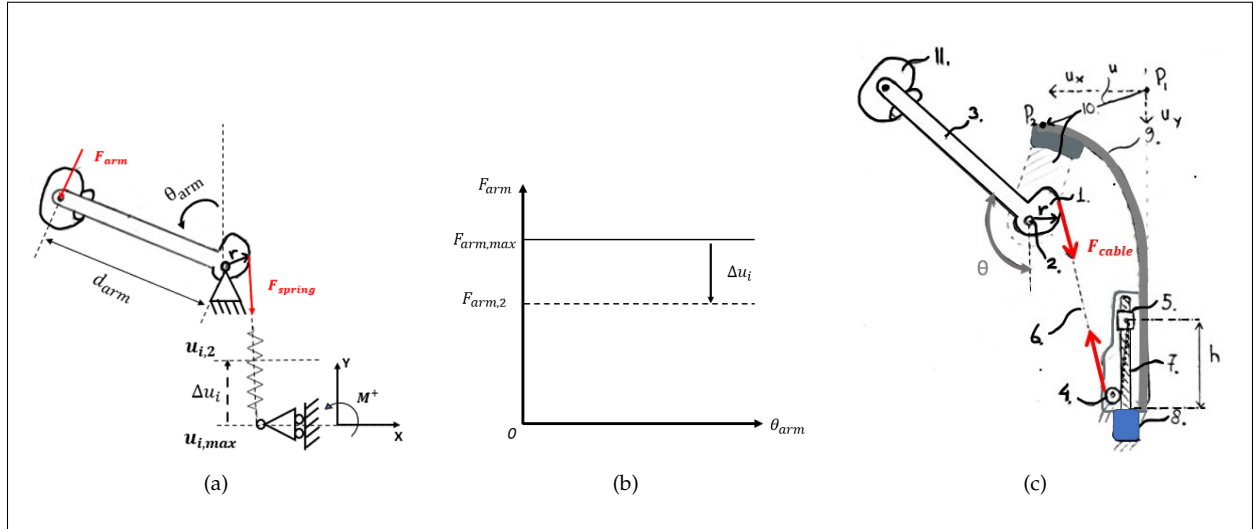
Figure 5: Principles of the constant force concept. **(a)** Schematic representation of the CAM concept. The radius of the CAM is represented by r, the length of the arm link is referred to as d_{arm}, the pretension for the maximum assistance force is referred to as $u_{i,max}$, the pretension for the adjusted assistance force is referred to as $u_{i,2}$, and the change in pretension is referred to as Δu_i. **(b)** Schematic plot of the force-angle characteristic when the pretension has been changed from $u_{i,max}$ to $u_{i,2}$, by an amount of Δu_i. **(c)** Drawing of Concept III, in which: 1. the CAM, 2. the main hinge, 3. the arm link, 4. the base pulley, 5. the lead screw nut, 6. the steel cable, 7. the lead screw, 8. the actuator, 9. the leaf spring, 10. the shoulder piece, 11. the arm cup. The deflection of the leaf spring has been indicated by u, the radius of the cam by r, the rotation of the arm link by θ, and the height of the lead screw nut with h.

the pretension of the leaf spring could be altered by means of a lead screw nut (5.) to which the cable is attached and of which the height can be adjusted by a motor (8.) rotating a lead screw (7.). If the lead screw nut is rotated upward, the effective cable length between pulley (4.) and the CAM is reduced, and thus a higher support force will be present at the arm cup. If the lead screw nut is rotated downward, the effective cable length will increase and the support force will decrease.

3.1.5 Concept IV: Adjustable Pulley Link

In this concept, the support force of the exoskeleton can be actively controlled by means of a pulley with an adjustable diameter. In concept III, a CAM accounted for the increase in cable tension as a result of deflection of the leaf spring, thereby creating a constant force-angle characteristic. If a pulley is used with a constant radius, a force-angle characteristic will be present that is proportional to the force-deflection curve of the leaf spring (see Figure 6a-b). Since the pulley used in this concept has a radius that can be actively adjusted, the radius could be varied such that it accounts for the increase in spring force when the leaf spring is deflecting, and is therefore also capable of providing a constant force-angle characteristic as in Concept III. The radius of the adjustable pulley can also be altered in a way such that the conventional force-angle characteristic of the Skelex 360-XFR would be provided to the user. Thus, with the adjustable pulley, a mechanism has been obtained capable of inducing a variety of force-angle characteristics dependent on the user's needs.

In Figure 6c, the concept has been depicted as if integrated on the frame of the Skelex 360-XFR,

formed by the leaf spring (1.) and the shoulder piece (2.). A constant length steel cable (7.) is connected to the variable diameter pulley consisting of a rotatable housing (5.) and linear sliders (6.) with arc shaped blocks at their endpoints which guide the cable. The effective diameter of the pulley is formed by those guidance blocks, and can be adjusted by an externally driven rotation of housing (5.). As each slider contains a pin (indicated by the red dots in Figure 6c) that are positioned in the arc-shaped slots of housing (5.), a rotation of this housing forces the slider either outward or inward, depending on the rotational direction of the actuator (2.). A timing belt (4.) is responsible for the transmission of the actuator's rotation to the adjustable pulley. Because the cable's end is fixed to both the pulley and the base, a rotation of the arm link (8.) will cause an increase in the cable force F_{cable} and an increase in torque around the rotation point of the pulley. The magnitude of this torque is dependent on both the deflection of the leaf spring and the diameter of the pulley, and is transferred through the arm link (8.) and the arm cup (9.) as a support force on the user's arm.

3.2 Concept Selection

3.2.1 Selection Framework

The performance of each concept has been assessed using a number of performance criteria. Performance criteria construct a framework to assess the quality of a concept. These are not black/white as the design requirements, but characteristics that should either be minimized or maximized. The performance criteria for the concepts were: weight, size, force adjustability, power consumption, durability, and feasibility.
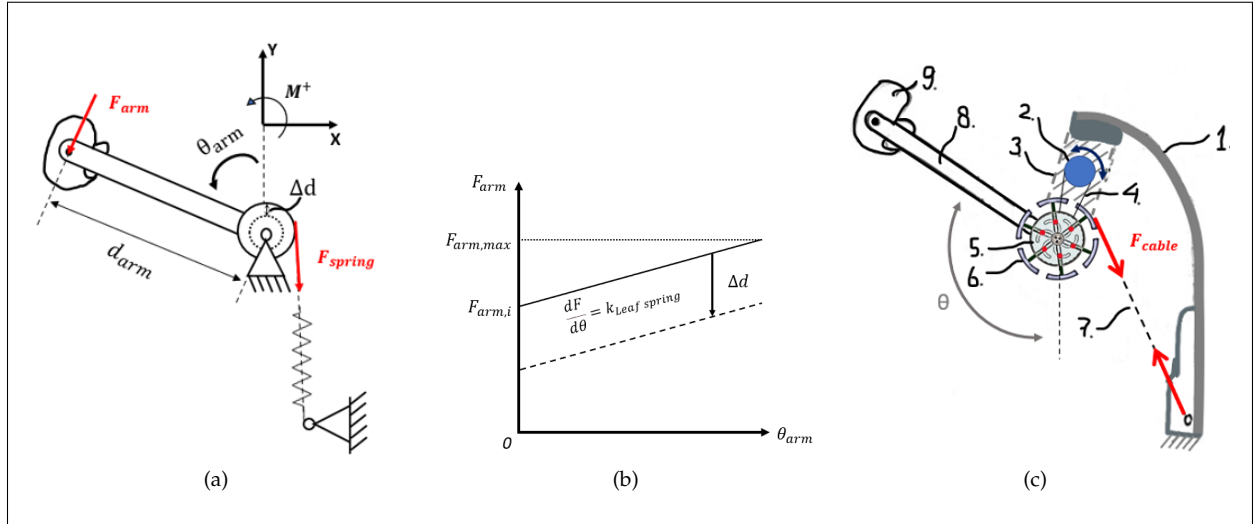
Figure 6: **(a)** Schematic representation of the adjustable pulley concept. The change in diameter due to actuation is indicated by Δd, the length of the arm link is referred to as d_{arm}, and the rotation of the arm link is indicated by θ_{arm}. **(b)** Schematic plot of the force-angle characteristic, when the diameter of the pulley remains the same during rotation. When the diameter changes by Δd, this results in a shift of the curve proportional to Δd. The angle of the force-angle characteristic is proportional to the stiffness of the leaf spring. **(c)** Drawing of Concept IV, in which: 1. the leaf spring, 2. an actuator, 3. the shoulder piece, 4. a timing belt, 5. the actuated part of the pulley, with arc shaped slots, 6. guidance blocks that form the effective diameter of the pulley, 7. a steel cable, 8. the arm link, 9. the arm cup.

These criteria have been used in combination with a weighted objectives table to derive the best performing concept. The principle of this selection method is as follows:

Every performance criterion on which the concepts have been graded are assigned with weights. The weights range from 1 to 3, where 1 is regarded as a relatively non-important requirement and 3 as a relatively important requirement. After weights have been assigned to each criterion, a grading system has been constructed such that the performance of each concept could be graded regarding the criteria. The grades range from 1 to 5, where 1 is regarded as very poor, 2 as poor, 3 as satisfactory, 4 as good, and 5 as very good. The grade of each criterion has been multiplied by the weights assigned to it, and this has been summed to end up with a total grade for each concept. The concept with the highest overall grade is regarded as the best performing concept and hence further developed.

3.2.2 Assessment Description

For each performance criterion, a brief explanation will be provided regarding the grades of each concept to ultimately end up with a total grade. The complete weighted objectives table has been presented in Table 1.

Weight. Weight has been assessed from two angles, firstly the absolute expected magnitude of the exoskeleton's weight, and secondly the location of weight in the exoskeleton. For example, if a weight of 2 kg is placed around the shoulder part of the exoskeleton this will be transferred through the entire upper body of a user, which is more intensive than when it would have been located around the hip

part of the exoskeleton. Concept I performs "good" as it contains only one actuator and relatively few components. Concept II performs "poor" as it contains two actuators, both located around the shoulder part of the exoskeleton. Concept III performs "very good", since its actuation mechanism, consisting of only one actuator, is located around the hip part of the exoskeleton and because it contains relatively few components. Concept IV performs "satisfactory", because it contains one actuator but relatively many components.

Size. Size is assessed based on the expectation of the largest protruding distance from the body. The

Table 1: Weighted objectives table, with weights ranging from 1 (relatively non-important) to 3 (relatively important) and grades based on a scale from 1 (very poor) to 5 (very good).

	Weights	Concept I: Parallelogram Linkage	Concept II: 2-drive Linkage	Concept III: CAM Link	Concept IV: Adjustable Pulley Link
Weight	3	4	2	5	3
Size	3	4	1	5	3
Force adjustability	3	5	5	2	2
Power consumption	2	5	1	5	2
Durability	1	4	3	5	1
Feasibility	1	4	3	5	1
Total:		57	32	56	30

more a concept is expected to protrude from the body, the lower the grade. Concept I performs "good", because the mechanism can be designed relatively close to the body. Concept II performs "very poor", because it requires two actuators that will result in a larger design, protruding more from the body. Concept III performs "very good", because the actuator is located around the hip joint, where more space is available to correctly position the parts in a way that minimizes the largest protruding dimension. Concept IV performs "satisfactory" because it contains a relatively high number of components that are mostly located around the shoulder joint, expected to result in a relatively large protruding dimension.

Force adjustability. The force adjustability is assessed based on the range of forces that can be provided by each conceptual mechanism. The higher the providable range of support forces, the higher the grade. Concept I and Concept II perform "very good", because the use of phase shifts makes it possible to reach any support force below the maximum support force that can be provided by the leaf spring. Concept III performs "poor", because it adjusts the support force only based on variations in pretension of the spring, limiting the lowest support force that can be provided to the user (misalignment between the main hinge of the mechanism and the natural shoulder joint will increase when the pretension is reduced, limiting its functionality). Concept IV performs "poor" too, as the lowest support force that can be provided to the user will be relatively high because the effective diameter of the pulley has a minimum.

Power consumption. Power consumption is assessed based on the expectation of the highest amount of force/torque necessary to alter the amount of support force in the ROM of the mechanism. Concept I performs "very good", because it is expected that the power consumption can be brought to a minimum based on a force-balancing principle. Concept II performs "very poor", because it makes use of two actuators. Concept III performs "very good", because also here it is expected that the power consumption of the actuator can be brought to a minimum based on force-balancing. Concept IV performs "poor", because it is expected that force-balancing will be relatively complex because of the complex design.

Durability. Durability is assessed based on the amount of moving components in each conceptual mechanism. The higher the number of moving components, the higher the probability that failure of one of these components will occur. Concept I performs "good", as it contains relatively few components, and because the loads in these components are brought to a minimum with the use of force-balancing. Concept II performs "satisfactory", because it contains more moving components compared to concept I. Concept III performs "very good", as this concept is the simplest design containing the lowest number of components. Concept IV performs "very poor", because this is the most complex design with the highest number of components.

Feasibility. Feasibility is assessed based on the expectation of the complexity in design and construction. Concept I performs "good", as the design is relatively simple, but does contain a few design challenges. Concept II performs "satisfactory", because a double actuation mechanism must be implemented, thereby increasing the complexity of the design. Concept III performs "very good", because this is the simplest design to construct. Concept IV performs "very poor", because of its complexity and high number of components.

As observable in Table 1, the overall grades of the parallelogram linkage concept (Concept I) and the CAM link concept (Concept III) differ by only 1 point, making it necessary to induce additional comparison criteria. Although it was not considered as a design requirement, it was preferred by Skelex B.V. that a potential solution would base its active alternations in support force on a mechanism involving active variations of an effective lever arm, as this involves an existing patent [7]. The driving mechanism of Concept I has a direct influence on an effective lever arm, whereas the driving mechanism of Concept III merely influences the pretension of the leaf spring. Another limiting factor of Concept III is the appearance of a misalignment between the shoulder joint of a user and the main hinge of the mechanism when the pretension of the leaf spring is minimized, limiting the lowest support force that can be provided to the user. Lastly, Concept III involves a mechanism that converts the typical force-angle characteristic into a constant force-angle characteristic, which is of advantage regarding the control of the support force, but of disadvantage when the suit is desired to be used in passive mode. The constant force-angle characteristic provided by the CAM is not effective as a passive gravity compensation, as the moment induced by gravity around the shoulder is dependent on the angle of the arm and thus not constant. The combination of the differences in correlation with the existing patent [7], minimum providable support force, and effectiveness in passive mode has formed the decision to further develop the Parallelogram Linkage concept (Concept I) instead of the CAM link concept (Concept III).

3.3 Analysis & Optimization

3.3.1 Overview

To provide an actively adjustable support force to the user during a task, implementation of an actuator is unavoidable. To optimize the performance of the design regarding criteria such as weight, dimensions, and power consumption, a process has been conducted with which the output torque of a motor is minimized. Firstly, the forces in the linkage mechanism are analysed to derive the expression of the reaction force between the lead screw and lead screw nut.

Secondly, the output torque is computed as a function of the derived reaction force. Thirdly, to minimize the maximum magnitude of required output torque, an optimization process is conducted based on a force-balancing principle. Ultimately, these steps lead to a predicted balancing spring stiffness that results in a minimum required output torque of the actuator.

3.3.2 Force Analysis Linkage Mechanism

For the force analysis of the parallelogram linkage, Free Body Diagrams (FBDs) are used of both the linkage mechanism as a whole (see Figure 7a) and the individual links (see Figure 7b). The first step of the force analysis was the computation of the support force exerted on the arms (F_{arm}) as a function of the force in the cable resulting from a deflection of the leaf spring (F_{cable}). It was assumed that the linkage mechanism, as depicted in Figure 7a, has a constant internal configuration (γ_{plg} = constant) as presented by the black triangles. Using the fact that, for static balance, the moments around main hinge R sum up to a total of zero, enables the computation of F_{arm} as a function of F_{cable} as in Equation 1.

$$\sum M_R = 0 \rightarrow F_{arm} = \sin\theta_{cable} \cdot F_{cable} \cdot \frac{d_{lever}}{d_{arm}} \quad (1)$$

In which:
- θ_{cable}, the angle between the lever arm and the cable.
- d_{lever}, the distance from the cable interface to the main hinge R.
- d_{arm}, the distance from the arm cup to the main hinge R.

With the force exerted by the user's arms on the arm link expressed as a function of both the cable force (F_{cable}) and the balancing force induced by the implemented zero-free-length spring (F_{spring}), it became possible to compute the forces transferred through the linkages to the lead screw (F_{Ls}) as a function of both F_{cable} and F_{spring}. The first step in the derivation of F_{Ls} was the computation of its first component, $F_{Ls,II}$ (see Figure 7b (Lead screw)). When the entire mechanism, as depicted in Figure 7a, is in static balance, its individual components must be too. Using the fact that for static balance, $F_{Ls,II} = F_{Link,I}$, and that the moments around main hinge R in link I must add up to a total of zero (as computed in Equation 2), allows the computation of the first component of the reaction force on the lead screw, $F_{Ls,II}$, as a function of F_{cable} and F_{spring}.

$$\sum M_R = 0 \rightarrow -F_{arm} \cdot d_{arm} + \sin\phi \cdot F_{link,I}$$
$$\cdot d_1 + \sin\frac{\phi}{2} \cdot F_{spring} \cdot d_1 = 0 \quad (2)$$

In which:
- d_1, the length of the part of the arm link participating in the parallelogram linkage.

- ϕ, the internal angle of the parallelogram linkage between the (lever) arm link and its coupler link.

Inserting Equation 1 in Equation 2 and solving for $F_{link,I}$ results in the expression of the first component of the reaction force on the lead screw, as computed by Equation 3.

$$F_{Ls,II} = F_{link,I} = \frac{\sin\theta_{cable} \cdot F_{cable} \cdot d_{lever}}{\sin\phi \cdot d_1}$$
$$- \frac{\sin\frac{\phi}{2} \cdot F_{spring}}{\sin\phi} \quad (3)$$

The second component of F_{Ls} is induced by link III, as depicted in Figure 7b, and is referred to as $F_{Ls,III}$. A similar approach as in the derivation of $F_{Ls,II}$ is used, where in this case $F_{Ls,III}$ is derived by making use of the fact that, for static balance, $F_{Ls,III} = F_{link,IV}$, and the sum of moments around main hinge R of link IV in Figure 7b must add up to a total of zero (see Equation 4).

$$\sum M_R = 0 \rightarrow \sin\theta_{cable} \cdot F_{cable} \cdot d_{lever} -$$
$$\sin\frac{\phi}{2} \cdot F_{Spring} \cdot d_2 - \sin\phi \cdot F_{link,IV} \cdot d_2 = 0 \quad (4)$$

In which:
- d_1, the length of the part of the arm link participating in the parallelogram linkage.

Solving Equation 4 for $F_{link,IV}$ results in the expression of the second component of the reaction force on the lead screw, as computed by Equation 5.

$$F_{Ls,III} = F_{link,IV} = \frac{\sin\theta_{cable} \cdot F_{cable} \cdot d_{lever}}{\sin\phi \cdot d_2}$$
$$- \frac{\sin\frac{\phi}{2} \cdot F_{Spring}}{\sin\phi} \quad (5)$$

With both components of the reaction force on the lead screw computed, it became possible to combine these into one expression for F_{Ls}, as in Equation 6.

$$F_{Ls} = \cos\frac{\gamma_{plg}}{2} \cdot (F_{Ls,II} + F_{Ls,III}) \quad (6)$$

Inserting Equation 3 and Equation 5 in Equation 6 results in the computation of F_{Ls} as a function of parameters of which the domains are known (see Equation 7).

$$F_{Ls} = \cos\frac{\gamma_{plg}}{2} \cdot \left[\frac{\sin\theta_{cable} \cdot F_{cable} \cdot d_{lever}}{\sin\phi} \cdot \left(\frac{1}{d_1}\right.\right.$$
$$\left.\left. + \frac{1}{d_2}\right) - \frac{2 \cdot F_{Spring} \cdot \sin\frac{\phi}{2}}{\sin\phi}\right] \quad (7)$$

As it is preferred to compute F_{Ls} in merely γ_{plg}, instead of a combination with ϕ, Equation 7 has been transformed to Equation 8 (given the fact that $\phi = \pi - \gamma_{plg}$).
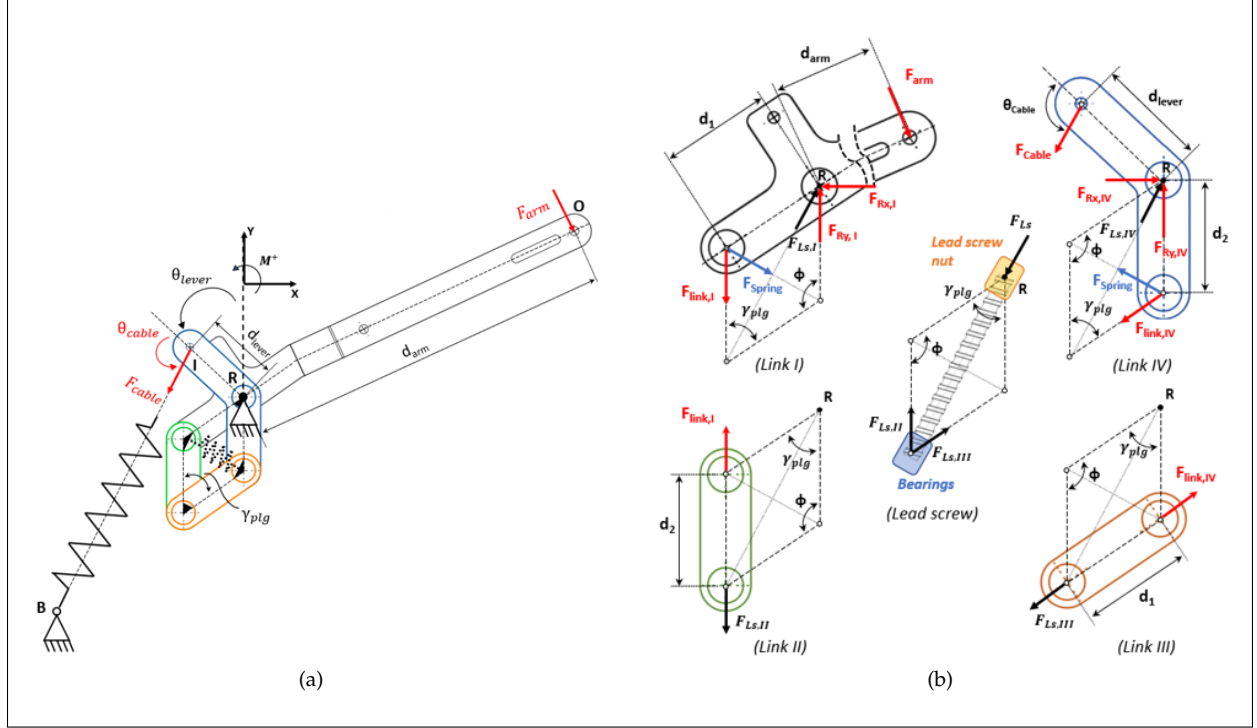
Figure 7: **(a)** Presentation of the parallelogram linkage mechanism in a configuration where the angles between the links remain static, as indicated by the black triangles. The mechanism acts as a rigid structure that has a rotational DOF around main hinge R. A rotation of the mechanism is defined by θ_{lever} and is measured with respect to the vertical. A spring force, transferred through a cable and referred to as F_{cable}, is acting on a lever arm with a length defined by d_{lever}. A reaction force of the user's arm (F_{arm}) is present at the arm link at a distance d_{arm} from main hinge R. The passive power source of the Skelex 360-XFR has been simplified represented by a tension spring, attached to a base B. Note: since the internal angle of the linkage is in this case assumed to remain static, the actuation mechanism (including a lead screw) has not been presented here. **(b)** FBDs of the individual linkages that combined form the parallelogram linkage, as in (a). (Link I) represents the arm link. (Link II) represents the coupler link of the arm link, in which $F_{link,I} = F_{Ls,II}$. (Link III) represents the coupler link of the lever arm link, in which $F_{link,IV} = F_{Ls,III}$. (Link IV) represents the lever arm link. (Lead screw) represents the lead screw, including its housing containing bearings and a lead screw nut.

$$F_{Ls} = \cos\frac{\gamma_{plg}}{2} \cdot \left[\frac{\sin\theta_{cable} \cdot F_{cable} \cdot d_{lever}}{\sin\gamma_{plg}} \cdot \left(\frac{1}{d_1} \right. \right.$$
$$\left. \left. + \frac{1}{d_2} \right) - \frac{2 \cdot F_{Spring} \cdot \cos\frac{\gamma_{plg}}{2}}{\sin\gamma_{plg}} \right] \quad (8)$$

3.3.3 Torque Output Derivation

The torque required to rotate a nut over a lead screw is dependent on: the direction and magnitude of the force acting between the nut and the lead screw, the friction coefficient between the nut and the lead screw, the diameter of the lead screw, and the lead of the lead screw. Two equations exist that describe the magnitude of the torque required to raise or lower a nut on a lead screw, as in Equation 9 and Equation 10, respectively [2]. These relations have been used to derive the magnitude of torque required to rotate the lead screw in the parallelogram linkage for any type of configuration.

$$T_{raise} = \frac{-F_{Ls} \cdot d}{2} \cdot \left[\frac{L + \mu \cdot \pi \cdot d}{\pi \cdot d - \mu \cdot L} \right] \quad (9)$$

$$T_{lower} = \frac{-F_{Ls} \cdot d}{2} \cdot \left[\frac{\mu \cdot \pi \cdot d - L}{\pi \cdot d + \mu \cdot L} \right] \quad (10)$$

In which:
- F_{Ls}, is the reaction force on the lead screw exerted by the lead screw nut in Nm.
- d, is the diameter of the lead screw in m.
- L, is the lead of the lead screw in m.
- μ, is the friction coefficient between the lead screw and lead screw nut.

3.3.4 Optimization Torque Output

One of the criteria that determines the performance of the semi-passive shoulder exoskeleton is the power consumption of its active force adjustment mechanism. The lower the power consumption, the better the performance of the force adjustment mechanism. Since the force adjustment mechanism in the parallelogram linkage includes a lead screw, the required power of the actuator is directly related to the torque required to rotate that lead screw. So when a low power consumption is desired, the maximum magnitude of the torque required to rotate the lead screw must be minimized. As observable from Equation 9 and Equation 10, the torque required to rotate the lead screw is a function of the reaction force (F_{Ls}) acting on it. Thus, minimizing the maximum magnitude of the reaction force that could act on the lead screw, means that the maximum magnitude of torque required to rotate it is minimized

as well.

The reaction force on the lead screw (F_{Ls}), as computed by Equation 8, is influenced by three variables: the angle of the cable with respect to the lever arm (θ_{cable}), the internal angle of the parallelogram linkage (γ_{plg}), and the stiffness of the balancing spring (k). The parameter F_{cable} is proportional to θ_{cable} and has been derived from the measured force-angle characteristic of the Skelex 360-XFR. The existence of these three variables and the measured parameter F_{cable}, made analytical computation of the stiffness k for which the maximum magnitude of F_{Ls} is minimized cumbersome. Therefore, an optimization process has been conducted with which the optimum value of k has been found and the maximum appearing magnitude of F_{Ls} is minimized, as mathematically described in Equation 11.

$$\min_{k} \max(|F_{Ls}(k)|), \ for \ \gamma_{plg} \ \in [40°, 140°] \cap \\ \theta_{lever} \in [-20°, 165°] \tag{11}$$

The scope of reaction forces that can act on the lead screw is defined by the domains of θ_{cable} and γ_{plg} ([-20°,165°] and [40°, 140°], respectively), the magnitude of the cable tension (F_{cable}) which has been derived from the (measured) force-angle characteristic of the Skelex 360-XFR, and the yet unknown stiffness k of the balancing spring. A 0th-order optimization [14] has been conducted, in which the goal of the first step was to find the rough location of the optimum, also referred to as bracketing. The brackets were in this case formed by the boundaries of a vector containing an increasing number of stiffness magnitudes. For each stiffness magnitude in this vector, the maximum magnitude of F_{Ls} has been computed and stored. Ultimately, the corresponding maximum magnitude of F_{Ls} was found for each stiffness. The stiffness with the lowest maximum magnitude of F_{Ls} was regarded as the optimum.

With the rough location of the optimum found, the boundaries of the vector containing the stiffness magnitudes have been shifted towards the earlier found optimum, referred to as sectioning. Reducing the magnitude of the steps between the components of that vector, resulted in a convergence point with a higher resolution. The optimization process was stopped when a convergence point with a resolution of 1 was found. Figure 8 depicts the last sectioning step that led to a convergence point with a stiffness $k = 1752 \, N/m$. As observable, the objective function $\max(|F_{Ls}(k)|)$ shows linear behaviour. This can be declared by taking a look at Equation 8. The left part of this equation is attributable to the reaction force occurring due to the tendency of the parallelogram linkage to collapse. This part is independent of the stiffness of the balancing spring, and will thus always have a constant maximum magnitude. The right side of Equation 8 is attributable to the balancing effect of the spring and is dependent on the stiffness. Since the
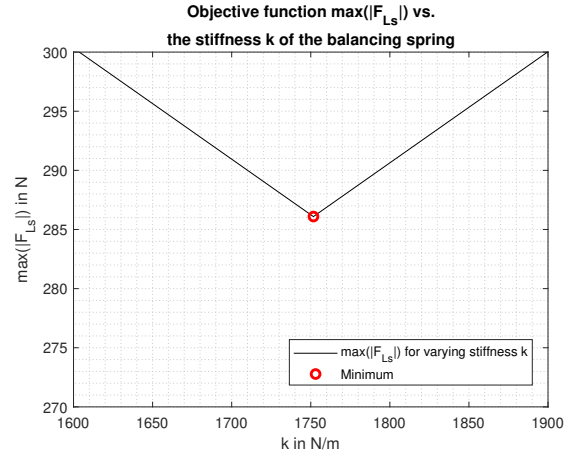

Figure 8: A visual presentation of the convergence point regarding the optimization process. The stiffness $k \approx 1752 N/m$ is resulting in the minimum value for the maximum magnitude of the reaction force on the lead screw $\max(|F_{Ls}|) \approx 286N$.

spring force is proportional to the spring stiffness, a change in stiffness results in a scaling of the right side of the formula. The maximum magnitude of the reaction force, thus, first decreases linearly until a point has been reached where the maximum reaction force's magnitude increases linearly again due to a too high balancing force. Based on the optimal balancing spring stiffness ($k = 1752 \, N/m$), the maximum magnitude of the required torque to rotate the lead screw will be: $\max(T_{Ls}) = 0.38 Nm$

3.4 Prototyping of the Phase Shifter

Based on the final concept and the findings by the model, a prototype has been designed, called the Phase Shifter. Figure 10 depicts both an isometric view of the whole mechanism and two detailed views of the parallelogram mechanism. When comparing it to the Skelex 360-XFR [18] (see Figure 1 and Figure 9), it is observable that the base of the two exoskeletons are similar, whereas the mechanisms between the arm and the base are differing. Essentially, the largest difference between both mechanisms is the type of adjustability. In the Skelex 360-XFR, the length of a lever arm can

Figure 9: The manufactured semi-passive prototype worn on the right arm versus the conventional passive exoskeleton worn on the left arm.
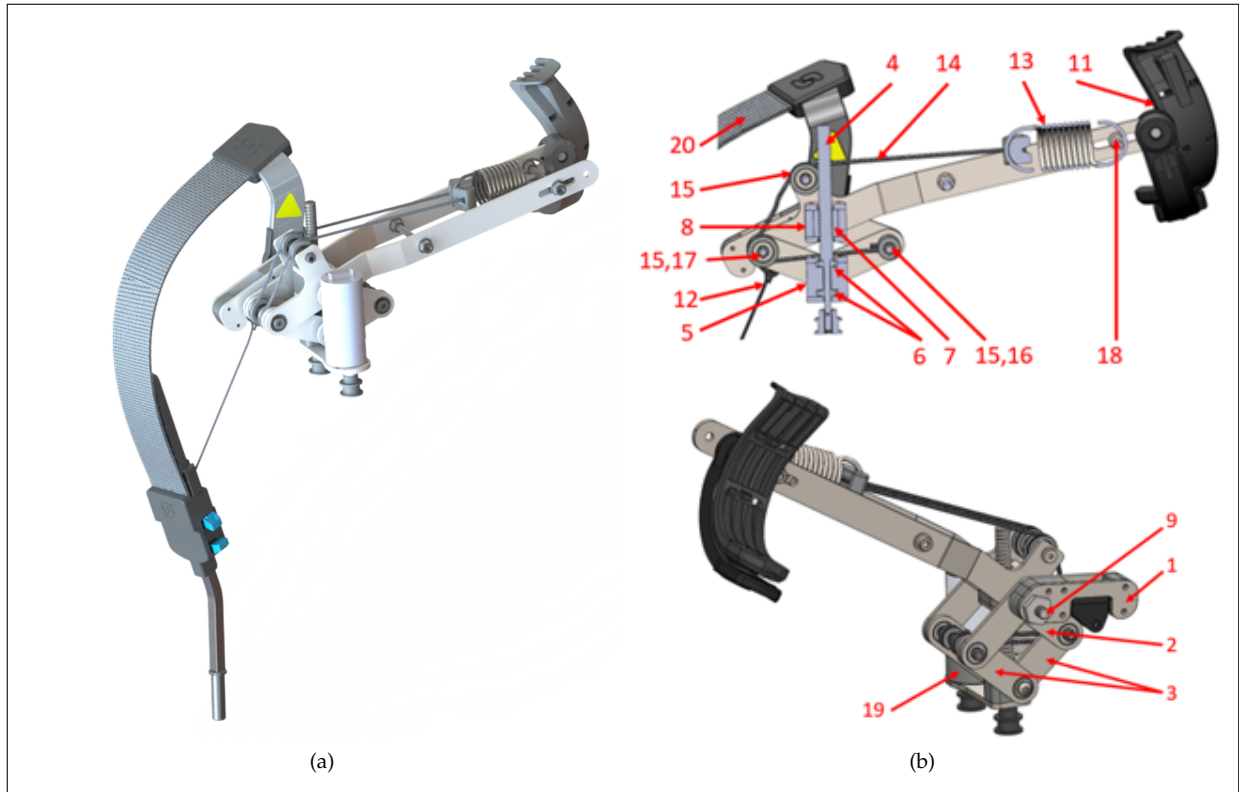
Figure 10: Schematic presentation of the Phase Shifter by an isometric view of the whole mechanism and a number of detailed views that indicate the position of the components. The numbers represent the components as follows: (1.) the lever arm link, (2.) the arm link, (3.) & (4.) the coupler links, (5.) housing of the ball bearings, (6.) the ball bearings, (7.) the lead screw nut, (8.) housing of the lead screw nut, (9.) the hinge pin, (11.) the arm cup, (12.) the steel cable, (13.) the balancing spring, (14.) the Dyneema cord, (15.) the pulleys, (19.) the DC motor, and (20.) the leaf spring. **(a)** Isometric view of the Phase Shifter. **(b)** Numbered detailed views of the Phase Shifter.

be manually adjusted, whereas in the Phase Shifter an angle between the input and output link can be actively adjusted. Thus, where the base stayed similar, still two completely different mechanisms are present. For now, attention will be paid mostly to the underlying working principle of the presented prototype in Figure 10.

The main functionality of the Phase Shifter is its ability to actively alter the angle between the lever arm link (1.) and the arm link (2.), and thereby also the phase of the force-angle characteristic. A parallelogram linkage has been formed by connecting two coupler links (3.) to each other, to the lever arm link (1.), and to the arm link (2.). A lead screw (4.) is placed on the diagonal of the parallelogram formed by the intersection of the arm- and lever arm link, and by the intersection of the two coupler links. The lead screw can 'lock' the parallelogram in certain configurations, as one side of the lead screw is clamped into a housing (5.) containing two ball bearings (6.) and the other side is constrained by a lead screw nut (7.) being fixed inside a second housing (8.). Both housings (5. & 8.) only have one rotational degree of freedom (DOF), such that the lead screw can always stay collinear with the diagonal of the parallelogram without being jammed. Since one side of the lead screw is fixed to the parallelogram in the housing (7.) containing the

bearings, and the other side is free to rotate through the housing (8.) containing the lead screw nut, a mechanism has now been obtained that can alter the internal angle of the parallelogram and thus also the angle between the arm and lever arm link by rotating this lead screw.

Just as in the Skelex 360-XFR, an in-going force induced by the leaf spring (20.) will be exerted on the lever arm link (1.) and because of the rotational degree of freedom of the entire mechanism around the main hinge (9.), an out-going force will be exerted on the users arms by the arm link. If no arm is present in the arm cup (11.), the mechanism will rotate back to a stable equilibrium point.

Both the force of the leaf spring exerted by the cable (12.) on the lever arm link, and the force of the arms exerted on the arm cup would normally result in the parallelogram to collapse. However, as there is a lead screw present between two collinear nodes of this parallelogram, this collapsing is prevented. As a result, however, a resultant force will be exerted at both nodes on the lead screw. Since at one of these nodes a housing is connected containing a lead screw nut and at the other node a housing containing ball bearings, only the housing containing the lead screw nut will be responsible for friction on the lead screw. Because the resultant force exerted by the lead screw nut on

the lead screw can reach values up to approximately 450 [N] (as calculated by Equation 8), high frictional forces will arise that result in high torques required to rotate the lead screw and change the relative angle between the links. As essential performance criteria are that the system must be lightweight and compact, high torques are undesired because this will result in a heavy and large motor. Therefore, a tension spring (13.) has been fixed to the arm link (which functions as a base) and to a Dyneema cord (14.) that is guided across the arm link by pulleys (15.) to nodes 16. & 17. of the parallelogram. When the parallelogram folds or opens, the spring is stretched in such a way that the resultant forces will be brought to a minimum for every possible configuration. So, where the external forces acting on the lever- and the arm link tend to fold the parallelogram linkage, the force induced by the integrated tension spring tends to open it, resulting in a balancing effect.

For the actuation of the Phase Shifter, a brushed DC motor (19.) has been used that has been attached to the lead screw by means of two pulleys and a timing belt. The direction and speed of the motor are controlled by a (on-off-on) toggle switch and a voltage controller, respectively. The power supply of the motor comes from a lithium-ion battery. The specifications of the main components used in the Phase Shifter are as follows:

- **Tension spring (Tevema T43090)**: This spring has a stiffness of 4010 [N/m] and a maximum allowable elongation of 98.06 [mm]. The characteristics of this spring are not ideal, as it was ordered under an early version of the model that contained some errors. Because of long lead times, it was necessary to integrate this spring in the prototype. Yet, this had no influence on the quality of the experiments, since all the hypotheses could still be validated properly.
- **Brushed DC motor (Modelcraft RB350018-2A723R 12 V 18:1)**: A motor has been chosen with torque output specifications that are well above the expected torque output belonging to the optimal stiffness. The quality of the experiment would have been affected if the motor had not been able to apply the required output torque on the lead screw. The exact relevant specifications of the motor are: max torque output (τ_{max}) = 2.06 [Nm], angular velocity (under load) (ω_{max}) = 317 [rpm], dimensions (Ø x l)= 36 [mm] x 101.6 [mm], weight = 0.35 [kg].
- **Battery (Team Corally Sport Racing 50C 6000mAh 3S 11,1V LiPo Battery)**: The battery is compatible with the DC motor being utilized and has a high capacity such that it could be used for a relatively long time.
- **Cord (S Core - Stirotex)**: A high tensile strength cord has been used that has a total length of 520 [mm] and a diameter of 3 [mm]. The maximum allowable load on this cord is 800 [kg].

- **Lead screw nut (IGUS - JSRM-C-01-TR10X3)**: A self-locking lead screw nut has been used that has a low friction coefficient and high durability. The friction coefficient of this nut is $\mu = 0.06 - 0.18$ under pure axial loading.
- **Lead screw**: A lead screw has been used that is made from C45 steel with a right metric thread of TR10x3.

4 EVALUATION
4.1 Experiment Design
4.1.1 Overview
To verify whether the expectations formed by the model regarding the resultant torque profiles of the lead screw and the optimal balancing spring stiffness are reliable, an experiment has been conducted. Furthermore, a second experiment has been conducted that intended to prove the working principle of the prototype (occurrence of phase shifts in the force-angle characteristic by folding and opening the parallelogram linkage). Folding of the linkage is characterized by an increasing value of its internal angle (γ_{plg}) and opening by a decreasing value of γ_{plg}.

4.1.2 Experiment Design for Validity Assessment of the Model
To prove the validity of the model, an experiment is conducted where the torque behaviour of the lead screw is measured during folding and opening movements of the parallelogram linkage for several starting configurations of the lever arm link ($\theta_{lever,i}$). The reason why different starting configurations of the mechanism have been tested, is that the starting angle of the lever arm ($\theta_{lever,i}$) directly affects the amount of deflection of the leaf spring (or the tension in the cable). As a result, the initial torques to rotate the lead screw and fold or open the parallelogram could be entirely different between two varying starting configurations of the lever arm. Getting a clear image of various expectations of the lead screw's torque behaviour versus its measured torque behaviour gives a more complete vision of the reliability of the model. To retrieve the desired torque output data, the experimental set-up as presented in Figure 11 has been used. The design of this set-up will be discussed in the remaining part of this section.

Firstly, a construction is made that could keep the arm link of the prototype at a pre-specified angle. In that construction, the prototype could be fixed at a position where the rotation point of the positioning mechanism was concentric with the rotation point of the prototype. An angle sensor (CMA-013i) was connected to the rotational axis of the positioning mechanism by means of a timing belt and two equally sized pulleys (1:1 transmission). This angle sensor could be read by software called Coach 7 and allowed to set the desired starting positions accurately by presenting the angle of the arm link on a monitor.
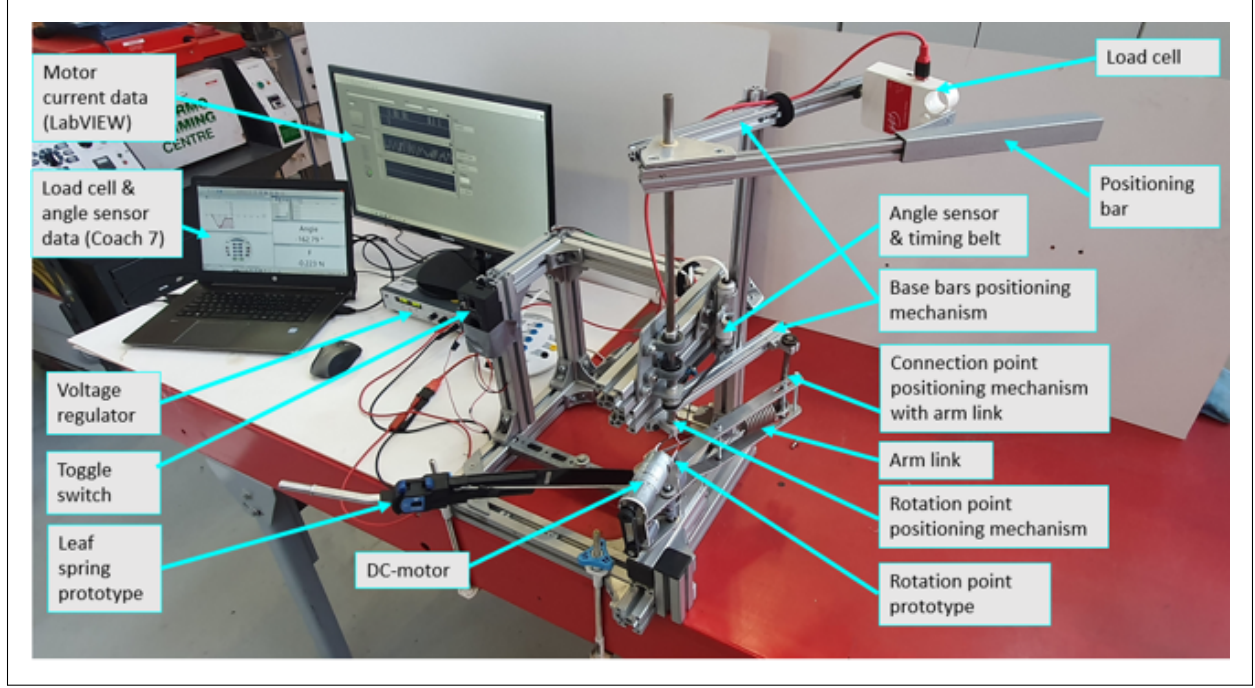
Figure 11: Set-up of the experiment. On the left top, the monitors are presented on which the data could visually be read. Underneath the large monitor, on which the current data has been presented, both a voltage regulator and the data acquisition (DAQ) units for the DC motor's current measurement are positioned. In the center of the picture, the test construction has been presented, in which the prototype has been placed. On the right upper side of this construction, an angle sensor has been mounted that measures the rotation of the arm link of the prototype. A load cell depicted in the upper right corner of the picture measures the support force of the exoskeleton that would normally act on the user's arms. Other aspects of the experiments can be found in the picture itself.

Besides the ability to precisely position the arm link of the prototype, another essential part of the experiment was to measure the torque profile of the lead screw during a full folding and opening movement of the parallelogram, with the angle of the arm link held constant. An important consideration was whether the measurement needed to be done dynamically or statically. It was decided to conduct a dynamic torque evaluation, as this approached the use case of the lead screw more closely. Since it is well known that the current consumption of a DC motor is proportional to its torque output [12], the motor itself could function as the (dynamic) torque sensor. The current consumption of the implemented DC motor has been read using an evaluation software called LabVIEW. The software could save the entire current usage during one trial and export it to a usable '*.txt file' that could be analyzed in MATLAB afterwards (see Appendix J). The block scheme used for the digital data conversion in LabVIEW can be found in Appendix G.

Before the experiment could be started, the DC motor's current-torque relationship needed to be established. This was done by an additional experiment (see Appendix H) where known incremental weights were attached to a cord that was wounded on a coil by rotating a DC motor. During rotation of this motor, its current consumption was measured. As both the radius of the coil and the weight attached to the cord were known, it was possible to calculate the torque corresponding to an average current consumption. It

was evident that a linear relation existed between the two, and hence a torque-current relation could be derived in the form of ($y = Ax + b$). The torque-current relation for the DC motor used in this experiment is presented in Equation 12.

$$T = 0.21897 \cdot I + -0.062622 \qquad (12)$$

With the torque-current relation for the DC motor used in the experiment established, the experiment could be initiated. Before a trial was started, the positioning mechanism was used to configure the prototype in the desired way. In total a number of 9 different starting configurations were investigated ($\theta_{lever,i} = 0°, 10°, 20°, 30°, 40°, 50°, 60°, 70°, 80°$), of which for each starting configuration 3 trials have been conducted. A trial involved keeping the arm link static at an angle dependent on: the starting configuration of the lever arm ($\theta_{lever,i}$), the initial internal angle of the linkage ($\gamma_{plg,i}$), and a constant related to the angles of the links themselves ($\theta_{arm} = (57° + \gamma_{plg,i}) - \theta_{lever,i}$), after which the DC motor was rotated in such a way that the parallelogram first folded and then opened again. The internal angle (γ_{plg}) of the point at which the parallelogram stopped was measured and documented. In the end, the parallelogram was again set at the initial internal angle ($\gamma_{plg,i}$) of 40 degrees, after which a new trial was started.

4.1.3 Experiment Design for Assessment of the Working Principle

To prove the working principle of the parallelogram mechanism, an experiment has been constructed where for a number of constant internal angles of the parallelogram linkage (γ_{plg}), full rotations are made with the arm link. The hypothesis was that a change in angle (or $\Delta\gamma_{plg}$) between the arm- and lever arm links would result in a phase shift of the force-angle curve (of the arm link) proportional to this change in angle. So, changing the internal angle of the linkage by, for instance, 10 degrees was expected to shift the force-angle curve with 10 degrees as well.

This experiment was conducted in the same construction as the model's validation experiment (see Figure 11), with as main difference the type of data being evaluated. Besides a positioning mechanism, the construction could also function as a force sensing mechanism by means of a load cell (CMA-BT42i) that has been placed between the positioning and base bars. This load cell therefore measures the exact load required to hold the arm link of the prototype at a specific position, and thus the amount of support force from the exoskeleton acting on the arm as well. Both the outgoing signals of the load cell and the angle sensor were processed by Coach 7. Plotting this data against each other resulted in the force-angle characteristics of the exoskeleton, hence making it possible to investigate potential phase shifts.

In total, a number of 6 varying internal angles of the parallelogram linkage (γ_{plg}) have been investigated ($40°, 60°, 80°, 100°, 120°, 140°$), of which $40°$ and $140°$ are the lower and upper limit of the folding range of the parallelogram, respectively. For each internal angle of the parallelogram, two trials were conducted. A trial consisted of firstly setting the internal angle of the parallelogram linkage to the value belonging to the trial by measuring it with a protractor, and secondly making a full rotation of the arm link back and forward by means of the positioning mechanism. After each trial, the data was stored by Coach 7 in a '*.csv' file such that it could be analysed in MATLAB afterwards (see Appendix K).

4.2 Results

4.2.1 Results of Validity Assessment Model

The experiment related to the validity assessment of the model has led to a total of 9 output torque profiles for both folding and opening movements of the parallelogram linkage, as presented in Figure 12 - Figure 14. Since folding and opening of the parallelogram linkage have an opposite effect on the rotation of the lever arm (as defined by θ_{lever}), the x-axes of the folding and opening plots are flipped compared to each other. So, when a folding motion is stopped at for instance $\theta_{lever} = 80$ degrees, the opening motion starts with $\theta_{lever} = 80$ degrees and runs back to the initial starting angle of the lever arm ($\theta_{lever,i}$) for that trial.

In the presented plots, the measured output torque profile of the DC motor based on the 3 conducted trials are presented by a mean (solid red line) and its standard deviation (red shaded region, with the bound represented by dashed lines). The original measured data appeared to be relatively noisy (see Appendix M) and hence has been filtered based on a moving average method. The goal of the experiment was to validate the predictions of the model. That is why, besides the measured output torque, also the predicted output torque of the DC motor is presented in these figures. This makes it possible to visually compare the fit of the predicted data with the measured (real) data and reason whether these predictions are valid or not.

The results as presented in this section are the results of a refined experimental process. An earlier experiment, of which the results are presented in Appendix D, has led to this refinement. Briefly mentioned, the differences between the original and refined experiment are: the number of trials that has been increased from 2 to 3 trials per starting configuration of the lever arm link, a number of mechanical improvements to the prototype that reduced both play around the main hinge and deflection of the base of the motor, and another DC motor that is used with a higher torque output and rotational velocity. For now, only the results of the refined experiment are of interest, as these are a better fit to the expectations as drawn by the model.

The following findings can be made from this experiment:

- For lever arm angles larger than $60°$, the deviation between the predicted torques and the measured torque region is mostly (close to) zero. For lever arm angles lower than $60°$, the deviation grows to an average of 0.1 Nm, where the shapes remain mostly similar.

- The peak torque predicted by the model is ≈ 0.41 [Nm] and the peak output torque measured from the DC motor is ≈ 0.52 [Nm]. This means that the model underestimates the peak in output torque by approximately 21 %.

- The underestimation of the model is mostly appearing in regions where the angle of the lever arm (θ_{lever}) is $\leq 60°$ and increases towards $0°$, especially for folding movements of the parallelogram linkage.

- Overestimations of the model are present as well, and mostly appear around regions where $\theta_{lever} \geq 60°$. Though, it is evident that the magnitude of these overestimations are lower compared to the magnitude of the underestimations.

- The measured output torque never hits the zero torque point, in contrast to what is expected by the model. Yet, the measured output torque profiles do show approximately the same minima at similar points compared to the predicted output torque. This is an indication of the presence of a radial force component at the lead screw nut,

causing a specific amount of friction, resulting in the DC motors output torque to always have a value greater than zero.

- The measured current consumption of the DC motor appeared to contain both noise and some periodicity, resulting in the measured torque patterns as presented in Appendix M. According to Vidlak et al. [20], the periodicity of a DC motor's current consumption is attributable to its AC-component, referred to as the ripple component. A self-conducted null-measurement (Appendix L) of the DC motor also showed that the noise and its periodicity are related to the DC motor itself. The digital filters show to filter out the noise and periodicity to a satisfactory extent.

4.2.2 Results of Working Principle Assessment

A second experiment was conducted to prove the working principle of the adjustment mechanism, which led to a total of 5 plots, as depicted in Figure 15. In the presented plots, a reference force-angle curve of the arm link is presented (blue dashed curve) together with a force-angle curve of the arm link related to a change in angle between the arm and lever arm link (black solid curve). The change in that angle is defined by the change in internal angle of the parallelogram linkage $\Delta\gamma_{plg}$. The reference force-angle curve is for each plot the same and is related to an internal angle of the parallelogram linkage of $\gamma_{plg} = 40°$. The phase of the measured curve compared to the reference curve is indicated by both an arrow and the magnitude of it.

It was expected that a change in relative angle between the arm and lever arm link by $\Delta\gamma_{plg}$ would lead to a proportional phase of the force-angle characteristic between both situations. Thus, when the internal angle of the parallelogram γ_{plg} is changed by $\Delta\gamma_{plg}$, the phase between the force-angle curves was expected to also be defined by $\Delta\gamma_{plg}$. In Table 2, the expected phase changes are compared to the phase changes derived from the measured force-angle curves. Analysis of the results as presented in Figure 15 and Table 2 have led to the following findings:

- From the presented plots, it is observable that the measured phase (ϕ) between the force-angle

curves show a somewhat proportional change with respect to $\Delta\gamma_{plg}$ for all the trials. The highest deviation between the expected and measured phase is $1.2°$ which is most likely related to a slight measurement error when the internal angle of the parallelogram was manually set using the protractor.

- The mechanism was prevented from getting into singularity by the interference of the lever arm with the cable, giving it the characteristic linear behaviour as shown in the plots of Figure 15. It is observable that this behaviour stops from an internal parallelogram angle of approximately 100 degrees. For internal angles larger than 100 degrees, no full rotations of the arm link could be made anymore, as observable from the plots as well.
- The shape of the force-angle curve stays the same throughout the varying phases.

4.2.3 Results of Design Requirements Assessment

To validate whether the prototype is a solution within the requirements as set at the beginning of the design phase, the prototype was assessed based on these requirements. It appeared that all functional requirements and constraints are met. Where some of the requirements could be assessed by simply looking at the features of the prototype, others had to be measured or tested. The results of these measured or tested requirements are discussed below:

- The smallest support force that can be provided by the prototype (for the largest distance to the main hinge) lies around 12 N, and can be provided up to an angle of 60 degrees with respect to the arms hanging vertically down.
- The weight of the total semi-passive exoskeleton, based on the prototype, is 4.59 kg, which is 0.41 kg lower than the initial requirement of 5 kg. The weight consists of two frames (2 x 1.84 kg), as presented in Figure 10, one battery (0.40 kg), and a harness (0.51 kg). Compared to the Skelex 360-XFR, which has a total weight of 2.9 kg, the semi-passive exoskeleton is 1.69 kg heavier.
- The maximum protruding dimension from the body is 145 mm in the coronal plane, which is 5 mm lower than the initial requirement of 150 mm.

Table 2: Results for the manually set internal angles (based on the protractor measurement of the parallelogram linkage) and the phases that have been derived based on the force-angle curves obtained by the load cell data versus the angle sensor data.

Change in relative internal angle $\Delta\gamma_{plg}$	Derived phase ϕ from measured force-angle curves
20°	21.2°
40°	39.7°
60°	58.8°
80°	80.9°
100°	99.1°

(a) Torque profiles for the folding movement of the parallelogram linkage, meaning that its internal angle (γ_{plg}) increases. The starting angle of the lever arm is $\theta_{lever,i} = 0°$.

(b) Torque profiles for the opening movement of the parallelogram linkage, meaning that its internal angle (γ_{plg}) decreases. The starting angle of the lever arm is $\theta_{lever,i} = 80°$.

(c) Torque profiles for the folding movement of the parallelogram linkage, meaning that its internal angle (γ_{plg}) increases. The starting angle of the lever arm is $\theta_{lever,i} = 10°$.

(d) Torque profiles for the opening movement of the parallelogram linkage, meaning that its internal angle (γ_{plg}) decreases. The starting angle of the lever arm is $\theta_{lever,i} = 90°$.

(e) Torque profiles for the folding movement of the parallelogram linkage, meaning that its internal angle (γ_{plg}) increases. The starting angle of the lever arm is $\theta_{lever,i} = 20°$.

(f) Torque profiles for the opening movement of the parallelogram linkage, meaning that its internal angle (γ_{plg}) decreases. The starting angle of the lever arm is $\theta_{lever,i} = 100°$.

Figure 12: Torque behaviour of the lead screw for folding and opening the parallelogram mechanism with starting angles of the lever arm of $\theta_{lever,i} = 0°, 10°, 20°$. Both the filtered measured data, represented by a mean (red solid line) and its standard deviation (red shaded region), and the calculated torque from the model (black solid line) have been represented. Above each figure, a title has been presented which states that both the folding and opening movement had the same starting angle. The reason for that is, although both plots are shown separately, they are both part of the same trial with the same starting angle of the lever arm ($\theta_{lever,i}$).
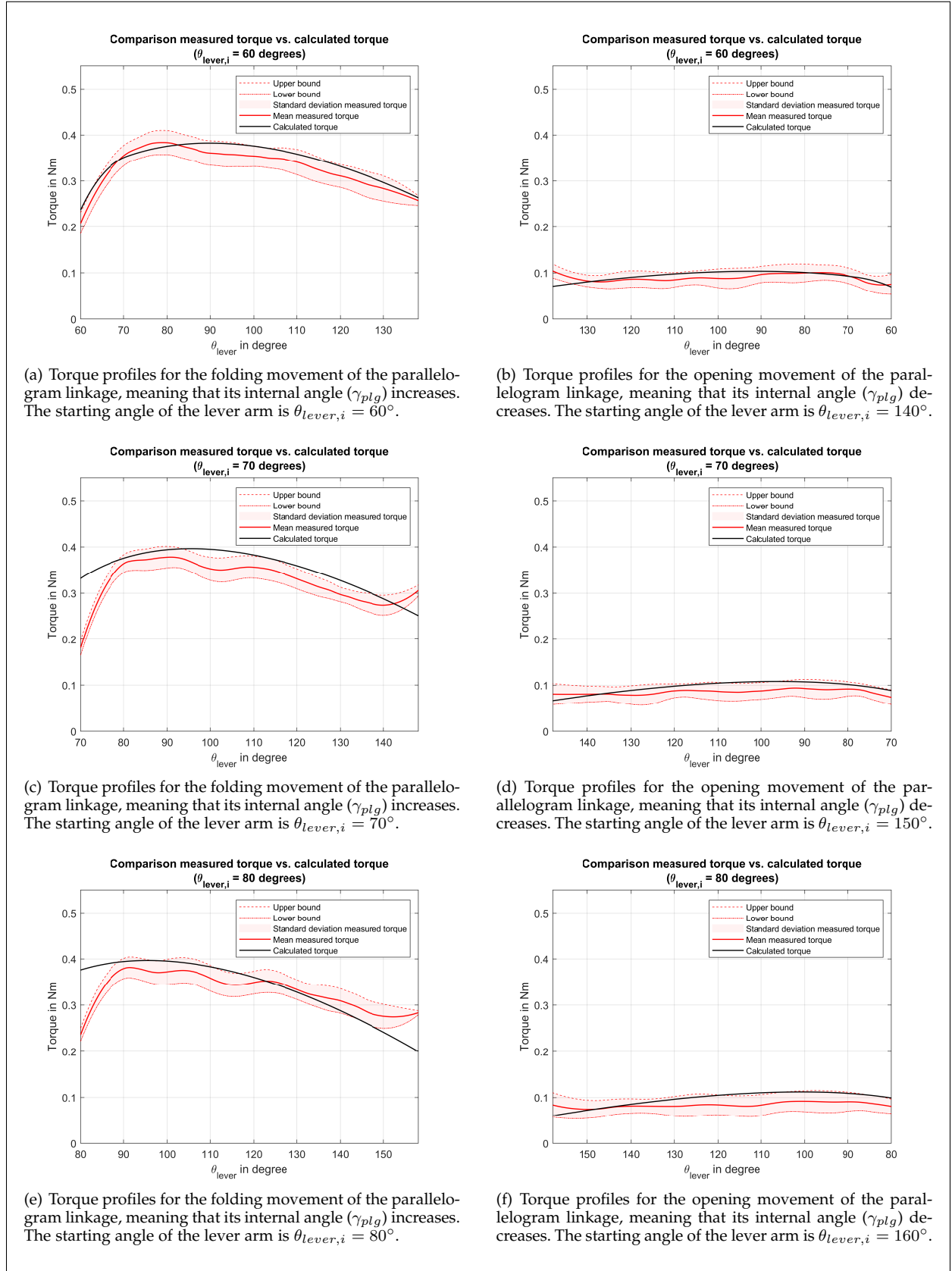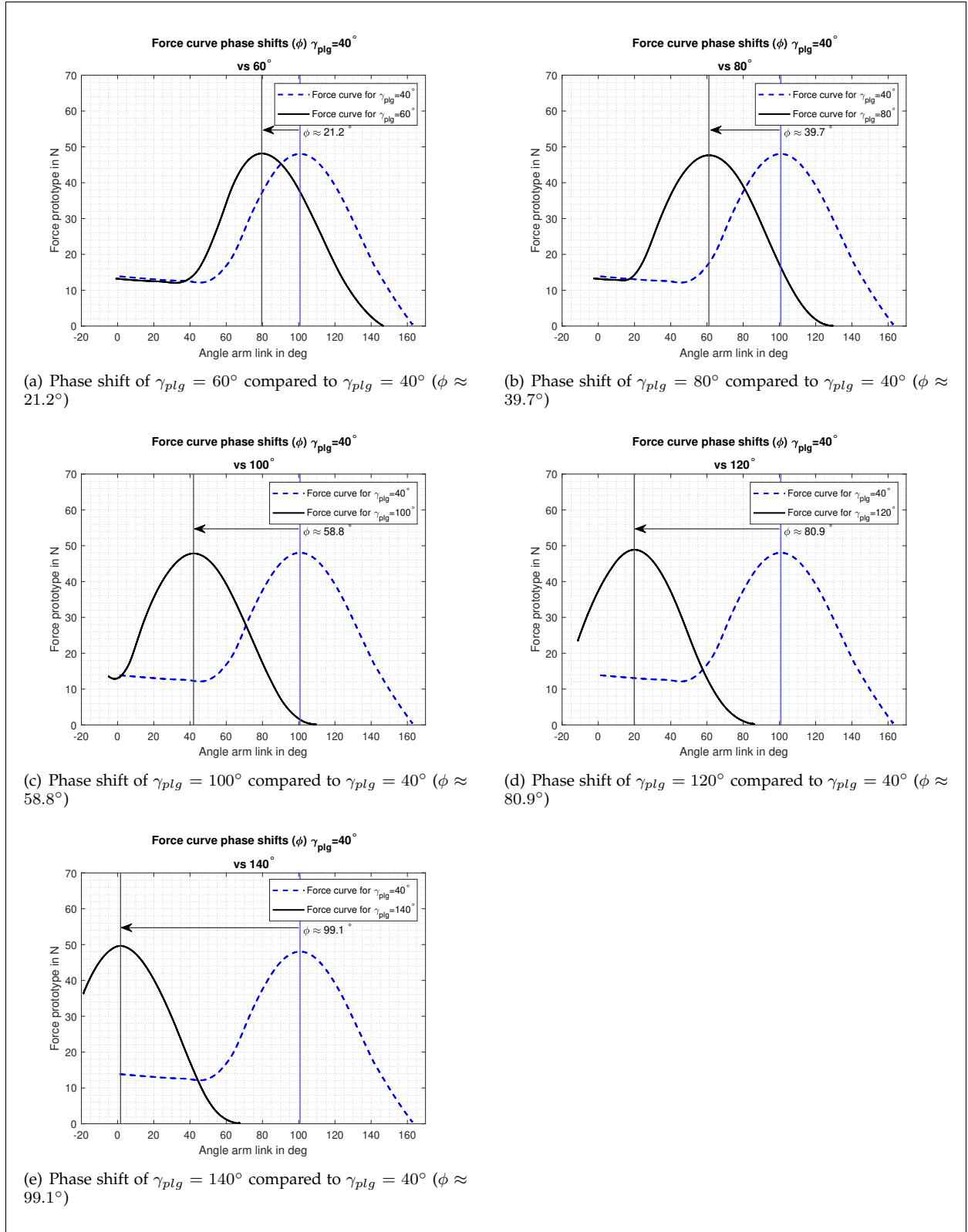
(a) Torque profiles for the folding movement of the parallelogram linkage, meaning that its internal angle (γ_{plg}) increases. The starting angle of the lever arm is $\theta_{lever,i} = 30°$.

(b) Torque profiles for the opening movement of the parallelogram linkage, meaning that its internal angle (γ_{plg}) decreases. The starting angle of the lever arm is $\theta_{lever,i} = 110°$.

(c) Torque profiles for the folding movement of the parallelogram linkage, meaning that its internal angle (γ_{plg}) increases. The starting angle of the lever arm is $\theta_{lever,i} = 40°$.

(d) Torque profiles for the opening movement of the parallelogram linkage, meaning that its internal angle (γ_{plg}) decreases. The starting angle of the lever arm is $\theta_{lever,i} = 120°$.

(e) Torque profiles for the folding movement of the parallelogram linkage, meaning that its internal angle (γ_{plg}) increases. The starting angle of the lever arm is $\theta_{lever,i} = 50°$.

(f) Torque profiles for the opening movement of the parallelogram linkage, meaning that its internal angle (γ_{plg}) decreases. The starting angle of the lever arm is $\theta_{lever,i} = 130°$.

Figure 13: Torque behaviour of the lead screw for folding and opening the parallelogram mechanism with starting angles of the lever arm of $\theta_{lever,i} = 30°, 40°, 50°$. Both the filtered measured data, represented by a mean (red solid line) and its standard deviation (red shaded region), and the calculated torque from the model (black solid line) have been represented. Above each figure, a title has been presented which states that both the folding and opening movement had the same starting angle. The reason for that is, although both plots are shown separately, they are both part of the same trial with the same starting angle of the lever arm ($\theta_{lever,i}$).

(a) Torque profiles for the folding movement of the parallelogram linkage, meaning that its internal angle (γ_{plg}) increases. The starting angle of the lever arm is $\theta_{lever,i} = 60°$.

(b) Torque profiles for the opening movement of the parallelogram linkage, meaning that its internal angle (γ_{plg}) decreases. The starting angle of the lever arm is $\theta_{lever,i} = 140°$.

(c) Torque profiles for the folding movement of the parallelogram linkage, meaning that its internal angle (γ_{plg}) increases. The starting angle of the lever arm is $\theta_{lever,i} = 70°$.

(d) Torque profiles for the opening movement of the parallelogram linkage, meaning that its internal angle (γ_{plg}) decreases. The starting angle of the lever arm is $\theta_{lever,i} = 150°$.

(e) Torque profiles for the folding movement of the parallelogram linkage, meaning that its internal angle (γ_{plg}) increases. The starting angle of the lever arm is $\theta_{lever,i} = 80°$.

(f) Torque profiles for the opening movement of the parallelogram linkage, meaning that its internal angle (γ_{plg}) decreases. The starting angle of the lever arm is $\theta_{lever,i} = 160°$.

Figure 14: Torque behaviour of the lead screw for folding and opening the parallelogram mechanism with starting angles of the lever arm of $\theta_{lever,i} = 60°, 70°, 80°$. Both the filtered measured data, represented by a mean (red solid line) and its standard deviation (red shaded region), and the calculated torque from the model (black solid line) have been represented. Above each figure, a title has been presented which states that both the folding and opening movement had the same starting angle. The reason for that is, although both plots are shown separately, they are both part of the same trial with the same starting angle of the lever arm ($\theta_{lever,i}$).

(a) Phase shift of $\gamma_{plg} = 60°$ compared to $\gamma_{plg} = 40°$ ($\phi \approx 21.2°$)

(b) Phase shift of $\gamma_{plg} = 80°$ compared to $\gamma_{plg} = 40°$ ($\phi \approx 39.7°$)

(c) Phase shift of $\gamma_{plg} = 100°$ compared to $\gamma_{plg} = 40°$ ($\phi \approx 58.8°$)

(d) Phase shift of $\gamma_{plg} = 120°$ compared to $\gamma_{plg} = 40°$ ($\phi \approx 80.9°$)

(e) Phase shift of $\gamma_{plg} = 140°$ compared to $\gamma_{plg} = 40°$ ($\phi \approx 99.1°$)

Figure 15: Results obtained by the phase shift experiment, shown with respect to each other. Note that $\gamma_{plg} = 40°$ is used as a reference to compare with the other internal angles (γ_{plg}) of the parallelogram. The hypothesis was that direct phase shifts would occur proportional to the change in γ_{plg}. So, in the case of a change from $\gamma_{plg} = 40°$ to $\gamma_{plg} = 60°$, a phase shift of $20°$ is expected.

5 DISCUSSION

5.1 Analysis & Interpretation

5.1.1 Validation of the Model

The reliability of the optimization process, and thus the model, was assessed by an experiment in which the current consumption of a DC motor was directly measured and converted into its torque output by using the derived current-torque relation of this DC motor. Since the model predicts the output torque based on an optimized balancing spring stiffness, a comparison between the predicted output torque profile and the measured output torque profile functioned as an assessment strategy for the reliability of the predictions of the model regarding the optimal force-balancing parameters.

It appeared that the torque output predictions of the model approached the measured torque output from the DC motor generally quite well for lever arm angles larger than $60°$, since the predicted torque profile lied mostly within the measured torque region. For lever arm angles lower than $60°$, the deviation between the predicted torque and the measured torque region increased to an average magnitude of 0.1 Nm, whilst the shapes between the curves remained mostly similar. The predicted peak torque value for the evaluated prototype was ≈ 0.41 Nm, where the measured peak torque that occurred was ≈ 0.52 Nm. This shows that the model underestimates the peak torque that would be required from the DC motor by approximately 21 %, which negatively influences the reliability of the model. From the experimental results, it has become evident that, in general, the model underestimates output torques for lever arm angles $(\theta_{lever}) \leq 60°$ and slightly overestimates output torques for lever arm angles $(\theta_{lever}) \geq 60°$.

The main reason for the underestimations by the model is expected to be the assumption that only axial loads are acting on the lead screw nut. In reality this has appeared not to be the case, as the measured output torque never approached zero when, theoretically, it had to. When the direction of the (axial) load on the lead screw nut changes, a point must be reached where the resultant force on the nut is zero (the static balance principle [10], [4]). Yet, in none of the situations where the direction of the load on the lead screw nut flipped, the measured output torque of the motor was (close to) zero. This indicates that, at these flipping points, a frictional force is still present. The existence of that frictional force means that the resultant force on the lead screw nut is not merely axial, but contains a radial component as well. It appears that this radial component increases when the lever arm rotates towards $0°$, where the cable tension is highest (see Figure 7b). So, the higher the deflection of the leaf spring (and thus the cable tension), the higher the radial force component on the lead screw nut, and the higher the underestimation of the output torque. High radial forces, thus, negatively influence the reliability of the model and must be prevented as much as possible.

Another limitation of the model is that its predictions are based on a static friction coefficient between the lead screw and lead screw nut, whereas in reality this is not the case. In the specifications, as presented in Appendix I, it has been indicated that the friction coefficient can vary between 0.06-0.18. The model only uses the friction coefficient in the 'worst case' of 0.18, resulting in overestimations when the friction coefficient appears to be lower in reality. It is expected that relatively low loads on the lead screw nut allowed the DC motor to spin faster, decreasing the dynamic friction coefficient, and thus leading to overestimations of the output torques at these points.

To conclude, under the assumptions that have been made regarding a static friction coefficient and the absence of radial load components between the lead screw and lead screw nut, the model can be regarded as valid. However, unless the relatively good approximation of the output torque magnitudes for lever arm angles larger than $60°$, the assumptions have shown to negatively influence the reliability of the model for the torque predictions for lever arm angles larger than $60°$. This has resulted in an underestimation of the predicted peak output torque of the actuator by 21%. If an actuator was selected based on the capacity as predicted by the model, it would not be able to provide enough torque to actuate the mechanism in extreme situations. Ultimately, the goal of the model is to predict the required capacity of the actuator, so every underestimation of the model regarding the maximum providable output torque of the actuator is unacceptable. Therefore, it is suggested that a penalty function is added in the model for lever arm angles lower than $60°$ that accounts for the underestimation of the model regarding the output torque as a result of radial loads.

5.1.2 Validation of the Working Principle

It was expected that a change in the angle between the lever arm link and the arm link of the parallelogram linkage, as represented by $\Delta\gamma_{plg}$, would result in a phase change of the force-angle curve proportional to $\Delta\gamma_{plg}$. From the experimental results, it is evident that the hypothesis is valid. Changes in relative angles led to proportional changes in phase shifts of the force-angle curve, with a maximum deviation of approximately 1.2 degrees. This deviation is attributable to measurement errors of the relative angle between the arm link and lever arm link, as these were set manually using a protractor.

5.2 Limitations

5.2.1 Limitations of the Design Strategy

The design strategy in this study involved the creation of concepts meeting the design requirements, after which a concept selection was done using a weighted objectives scheme to derive the best performing concept regarding the performance criteria. In total, four

concepts have been compared, out of which 2 concepts performed almost equally good (difference of 1 point). The decision was made to introduce additional criteria with which each concept has been assessed. The best performing concept regarding the additional criteria was regarded as the best solution to be further developed.

Reflecting on this process, the selection between the two concepts may have been done too early. Although it appeared that the parallelogram linkage concept performed better than the CAM link concept, a more well-argued decision could have been made by developing both concepts parallel to each other and testing their functionalities based on their prototypes. Yet, this would have interfered with the time management of the project, as the design of an additional prototype and evaluation method would have resulted in additional effort and time that was limitedly available for this study.

5.2.2 Limitations of the Prototype

The prototype used in the experiments was not yet provided with the most optimal components, because the balancing spring was ordered under an early version of the model containing a few errors, and the capacity of the actuator was selected with a safety factor as the reliability of the model was yet unsure. With the knowledge obtained from the experiments, it can be stated that when the predictions of the model regarding the spring stiffness and peak output torque of the actuator are used in a new component selection, this will result in the most optimal design regarding the design requirements. As an indication, a balancing spring with spring stiffness of $k = 4010$ [N/m] has been implemented in the prototype that has eventually resulted in a predicted peak output torque of the actuator of 0.41 [Nm]. If the optimized spring would be implemented (with a spring stiffness of $k = 1752$ [N/m]) the peak in output torque is expected to lie around 0.38 [Nm].

The difference between the predicted output torques is surprisingly minor because the balancing spring in the prototype has not fully been converted into a zero-free-length spring due to dimensional limitations. As a result, the spring had lower tension magnitudes for the same internal angle of the parallelogram linkage as if it was used as a zero-free-length spring. One might therefore argue that the use of a zero-free-length spring is not essential for the minimization of the required peak output torque of an actuator. Yet, not implementing a zero-free-length spring will cause problems whenever the fold range of the parallelogram is increased, since there will be points where the balancing spring is fully relaxed and thus not effective. Ultimately, that will result in high required output torques of the actuator. If the spring implemented in the prototype would have been used as a zero-free-length spring, the predicted peak output torque would have been 0.64 [Nm], indicating the

importance of the optimization process.

Another limitation of the prototype is that radial loads are still present at the lead screw nut. It has appeared that within each ball bearing a specific amount of play was present. That play caused uneven load distributions on the housing in which the lead screw nut has been located, and thus radial load components between the nut and the lead screw. To prevent radial loads acting on the lead screw nut, a more rigid design with less play and deflections should be made. Implementing this, is expected to increase the reliability of the model and to decrease the peak torque required to rotate the lead screw.

5.3 Recommendations

Based on the findings from this study, recommendations can be made regarding the design of the semi-passive exoskeleton itself, control strategies of the actuator, and other next steps for the company. A recommendation regarding the design of the semi-passive exoskeleton would be to further minimize its weight, dimensions, and torque output. This can potentially be achieved by the use of a customized balancing spring with a stiffness as determined by the model, a lead screw nut capable of handling radial loads, and a smaller actuator that still has enough capacity to drive the force adjustment mechanism.

Since this study is devoted to the mechanical design and optimization of the semi-passive exoskeleton, yet no attention has been paid to the control strategy of the actuator. A control strategy is suggested where the required support force, that minimizes the loads in the shoulder during a task, is actively sensed. Given the force-angle characteristic and the possibility to induce phase changes of that characteristic, enables actuation based on the required sensed magnitude of support force. The complexity of this strategy lies in the sensing method. Promising methods containing low noise and relatively high detection accuracies are force myography (FMG) based motion detection methods [6], [19], [17]. Combining angle sensors that determine the angle of the upper arm together with an FMG-based arm cup determining the magnitude of the required support force, could be an interesting sensing strategy for control of the semi-passive exoskeleton.

Experiments must be conducted to analyse the biomechanical effectiveness of this method, by making use of EMG sensors placed on the upper limb. In this way, the potential reduction in voluntary muscle contractions in a user's shoulder can be objectively derived from a comparison between the use of the passive and semi-passive exoskeleton. A second experiment should investigate the user experience of the semi-passive exoskeleton during a number of use cases by means of a questionnaire, for example. Combining objective and subjective results should create a clear image of the effectiveness of the semi-passive shoulder exoskeleton in reducing muscle activity in a user's shoulder.

6 CONCLUSION

In this study, the design of a low-power drivable mechanism has been presented to increase the range of providable support to a user when implemented on the same frame as the Skelex 360-XFR. The implementation of a drivable parallelogram linkage showed to effectively induce phase shifts of the conventional force-angle characteristic, and thus, to be capable of increasing the providable support force range. Furthermore, the implementation of a force-balancing strategy showed to effectively reduce resultant loads on the driving mechanism, thereby minimizing the power output, size, and weight of the required actuator. To conclude, this study's design process has successfully resulted in a drivable mechanism that, with the right control strategy, can increase the load reduction performance of the Skelex 360-XFR for dynamic tasks.

ACKNOWLEDGEMENTS

REFERENCES

[1] Lorenzo Aquilante, Tabaglio Mattia, and Danielle Ramirez. *Load compensation device, in particular of gravitational loads, applicable to exoskeletons*. July 2022. URL: https://worldwide.espacenet.com/patent/search/family/067998672/publication/US2022218552A1?q=Lorenzo%20Aquilante.

[2] Anton van Beek. *Advanced Engineering Design*. 2012. ISBN: 9789081040617.

[3] Branko Brackx et al. "Design of a modular add-on compliant actuator to convert an orthosis into an assistive exoskeleton". In: *5th IEEE RAS/EMBS International Conference on Biomedical Robotics and Biomechatronics*. IEEE, Aug. 2014, pp. 485–490. ISBN: 978-1-4799-3128-6. URL: https://ieeexplore.ieee.org/document/6913824.

[4] Luis F. Cardoso, Seťrgio Tomaťzio, and Just L. Herder. "Conceptual design of a passive arm orthosis". In: *Volume 5: 27th Biennial Mechanisms and Robotics Conference*. Vol. 5 B. American Society of Mechanical Engineers, Jan. 2002, pp. 747–756. ISBN: 0-7918-3653-3. URL: https://asmedigitalcollection.asme.org/IDETC-CIE/proceedings/IDETC-CIE2002/36533/747/295253.

[5] Bruno R da Costa and Edgar Ramos Vieira. "Risk factors for work-related musculoskeletal disorders: A systematic review of recent longitudinal studies." In: *American journal of industrial medicine* 53.3 (Mar. 2010), pp. 285–323. URL: http://www.ncbi.nlm.nih.gov/pubmed/19753591.

[6] Zhen Gang Xiao, Ahmed M Elnady, and Carlo Menon. *Control an exoskeleton for forearm rotation using FMG*. 2014. ISBN: 9781479931286.

[7] Gaurav Genani. *Force-Balancing Support, Mechanical Apparatus and Wearable Support Device*. Aug. 2019. URL: https://worldwide.espacenet.com/patent/search/family/057326447/publication/US2019240102A1?q=skel-ex%20holding.

[8] Lorenzo Grazi et al. "Design and experimental evaluation of a semi-passive upper-limb exoskeleton for workers with motorized tuning of assistance". In: *IEEE Transactions on Neural Systems and Rehabilitation Engineering* 28.10 (Oct. 2020), pp. 2276–2285. URL: https://ieeexplore.ieee.org/document/9159674/.

[9] Muhammad Ahsan Gull, Thomas Bak, and Shaoping Bai. "Dynamic modeling of an upper limb hybrid exoskeleton for simulations of load-lifting assistance". In: *Proceedings of the Institution of Mechanical Engineers, Part C: Journal of Mechanical Engineering Science* 236.5 (Mar. 2022), pp. 2147–2160. URL: http://journals.sagepub.com/doi/10.1177/09544062211024687.

[10] Justus Herder. "Energy-free systems : theory, conception and design of statically balanced spring mechanisms". PhD thesis. Delft: Delft University of Technology, Nov. 2001. ISBN: 90-370-0192-0.

[11] Marko Jamek, Tadej Petri, and Jan Babi. "Gaussian mixture models for control of quasi-passive spinal exoskeletons". In: *Sensors* 20.9 (May 2020), p. 2705. URL: https://www.mdpi.com/1424-8220/20/9/2705.

[12] G H Jang, J H Yeom, and M G Kim. "Determination of torque-speed-current characteristics of a brushless DC motor by utilizing back-EMF of non-energized phase". In: *Journal of Magnetism and Magnetic Materials* 310 (2007), pp. 2790–2792. URL: www.elsevier.com/locate/jmmm.

[13] Paolo de Leva. "Adjustments to Zatsiorsky-Seluyanov's segment inertia parameters". In: *Journal of Biomechanics* 29.9 (Sept. 1996), pp. 1223–1230. URL: https://linkinghub.elsevier.com/retrieve/pii/0021929095001786.

[14] Sijia Liu et al. "A Primer on Zeroth-Order Optimization in Signal Processing and Machine Learning". In: ().

[15] Michiel P. de Looze et al. "Exoskeletons for industrial application and their potential effects on physical work load". In: *https://doi.org/10.1080/00140139.2015.1081988* 59.5 (May 2015), pp. 671–681. URL: https://www.tandfonline.com/doi/abs/10.1080/00140139.2015.1081988.

[16] Francesco Missiroli et al. "Rigid, soft, passive, and active: a hybrid occupational exoskeleton for bimanual multijoint assistance". In: *IEEE Robotics and Automation Letters* 7.2 (Apr. 2022), pp. 2557–2564. URL: https://ieeexplore.ieee.org/document/9681209/.

[17] Vikram Ravindra and Claudio Castellini. "A comparative analysis of three non-invasive human-machine interfaces for the disabled". In: *Frontiers in Neurorobotics* 8 (Oct. 2014). URL: http://journal.frontiersin.org/article/10.3389/fnbot.2014.00024/abstract.

[18] *Skelex 360-XFR - Skelex*. URL: https://www.skelex.com/skelex-360-xfr/.

[19] Stefanou T et al. *Upper limb motion intent recognition using tactile sensing*. 2017. ISBN: 9781538626825.

[20] Michal Vidlak et al. "Sensorless speed control of brushed dc motor based at new current ripple component signal processing". In: *Energies* 14.17 (Sept. 2021). URL: https://www.researchgate.net/publication/354215563_Sensorless_Speed_Control_of_Brushed_DC_Motor_Based_at_New_Current_Ripple_Component_Signal_Processing.

[21] Asher Winter, Navid Mohajer, and Darius Nahavandi. "Semi-active assistive exoskeleton system for elbow joint". In: *2021 IEEE International Conference on Systems, Man, and Cybernetics (SMC)*. IEEE, Oct. 2021, pp. 2347–2353. ISBN: 978-1-6654-4207-7. URL: https://ieeexplore.ieee.org/document/9658720/.

Appendix A
Task Analysis

For the MATLAB script, see MATLAB code Task Analysis.

Appendix B
Leaf Spring Deflection Extremity
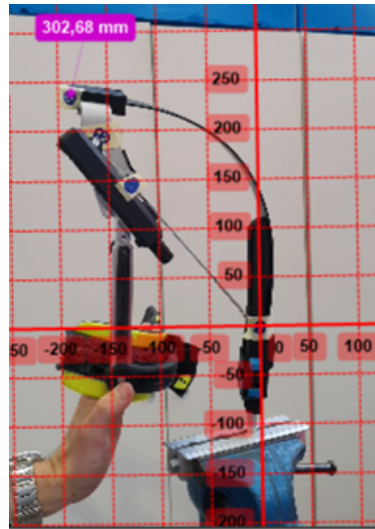
Figure 16: Video tracking configuration to derive the maximum allowable deflection of the leaf spring. For the video tracking, Kinovea video tracking software has been used. The tracked end node of the leaf spring has been indicated in [mm]. Both the x and y coordinates of this end node have been stored in a '*.csv' file and inserted in the MATLAB code.

For the MATLAB script, see MATLAB code Leaf Spring Deflection.

APPENDIX C
PROTOTYPE I
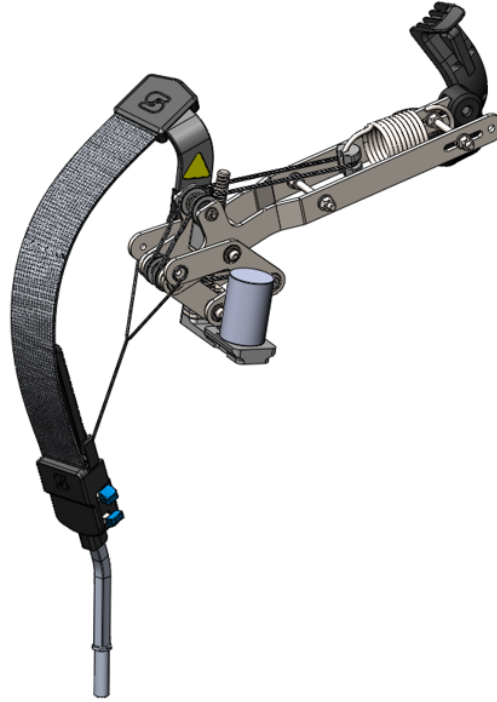
Figure 17: The isometric view of prototype I. The most important differences compared to the prototype discussed in Subsection 3.4 are: the base of the motor, which is a printed part in this prototype and an aluminum part in prototype II, the motor which has an increased torque output rotational velocity, and size in prototype II, the interface between the lever arm and the cable, which has a rotational DOF in prototype II, and the plain bearings (not visible) that have all been replaced by ball bearings in prototype II.

APPENDIX D
TORQUE EXPERIMENT I

D.1   Results

In total a number of 9 different starting configurations have been investigated ($\theta_{lever,i} = 0°, 10°, 20°, 30°, 40°, 50°, 60°, 70°, 80°$), of which for each starting configuration 2 trials have been conducted. The results have been plotted in Figure 18 - Figure 20. A few remarks need to be made regarding the results as presented in these plots:

- Two different lines have been plotted that both show the profiles of calculated resultant torques by the model. The reason for this is that, in the prototype, the cable is attached to the base at a different point compared to the Skelex 360-XFR. It has been shifted by $\approx$ 40mm to the inner side of the leaf spring. This has been done out of performance reasons. Attaching the cable at the initially designed place for it twisted the mechanism so much that it would not function as desired anymore. Furthermore, the cable interfered with the mechanism at a certain point, which limited the range of motion of the exoskeleton. By shifting the attachment to the base with $\approx$ 40mm inwards, this these problems have been solved.
  This, however, also resulted in a different bending behaviour of the leaf spring, and thus also a different cable tension at certain points. After a small test (where the cable tension was derived from load cell data related to the arm link's reaction force) it appeared that the shape of the force curve stayed approximately the same, but higher force values were achieved that lied approximately 6% higher compared to the original force curve (see Appendix E, Figure 21). So, the calculated torques that are the approximation of the torques in the prototype are referred to as 'Calculated Torque v2' and the reference torque behaviour if the cable would be attached to the originally designed place for it is referred to as 'Calculated Torque v1'.
- The measured torque data has been presented as a region defined by an upper and lower torque profile. This region defines the range in which the measurement related torque data lied and is thus a representation of the measurement deviation. A solid red line has been presented that lies within this region and represents the mean. The mean of the measurement data is ultimately regarded as the most reliable representation of the measured torque output of the actuator.

- The lines that define the measurement deviation and mean are all based on a filtered dataset of the measured output torque from the DC-motor. It has appeared that the raw data of the DC-motor's output torque was rather noisy and showed a certain periodicity. This has appeared to be mostly related to the DC-motor's 'natural' current consumption, as a null-measurement also showed this behaviour. It has therefore been decided to choose a significantly high filter parameter to account for this.
- Since folding and opening of the parallelogram linkage have an opposite effect on the rotation of the lever arm (as defined by θ_{lever}), the x-axes of the folding and opening plots are flipped compared to each other. So, when a folding motion is stopped at for instance $\theta_{lever} = 80$ degrees, the opening motion starts with $\theta_{lever} = 80$ degrees and runs back to the initial starting angle of the lever arm ($\theta_{lever,i}$) for that trial.

D.2 Discussion

As observable from Figure 18 - Figure 20, in some cases the model's predictions approach the measured values closely and in other cases the model's predictions are not reaching a satisfactory approach level. Several reasons for this are the following:

- The reason why, especially at lower values of θ_{lever}, the measured torques are underestimated by the model, is that the parallelogram mechanism had quite some play around the hinge pin. Because at these lower lever arm angles the deflection of the leaf spring, and thus the cable tension, is high, twisting of the mechanism appeared and resulted in an uneven load distribution across the lead screw nut. As the lead screw nut's frictional performance is degrading heavily under radial loading, it is expected that this is a major factor of the overshoots in torque of the measured data compared to the calculated data at these lower angles.
- Not only magnitude differences are present between the measured and calculated torques, but also some phase differences are observable. A reason for this could be that, especially at the lower values of θ_{lever} for the opening movement of the parallelogram linkage, the timing belt slipped over the pulleys. Slipping negatively affects the quality of the measured torque output, since slipping of the timing belt means that the internal angle of the parallelogram linkage was not adjusted. As the points at which slipping occurred have not been measured, the torque profiles are 'deformed' at these points.
- High data fluctuations (and thus large standard deviations) at, especially lower values of θ_{lever}, can also be declared by slipping of the timing belt over the pulley. This basically happened because the base of the motor has been 3D-printed out of a too flexible material. Due to the high loads at these smaller angles of the lever arm, the base piece bend and the timing belt slipped resulting in noisy, and thus not representable data. Moving average filters based on a relatively high data span have been applied to the raw data to account for these fluctuations.
- Another problem that arose due to slipping was that the range of opening and folding was limited. For lower starting angles of the lever arm ($\theta_{lever,i}$) the spring reached a high amount of deflection. Due to this high deflection, the required torque to rotate the lead screw increased until a point where the mechanism slipped. At this point, it was necessary to abort the trial, resulting in a lower overall folding range.

Overall, it can be stated that due to the high amount of limiting factors, the experiment is not representable enough to say something substantial about the validity of the model. It is observable though that for some regions in the plots, especially where balancing is most effective, the model approaches the torque patterns from the experiment quite closely. That is why it has been decided to build a second prototype, where iterations have been made to tackle the flaws that appeared from this experiment. In this way, hypotheses regarding the flaws recognized in this experiment and stated above can be verified or not.
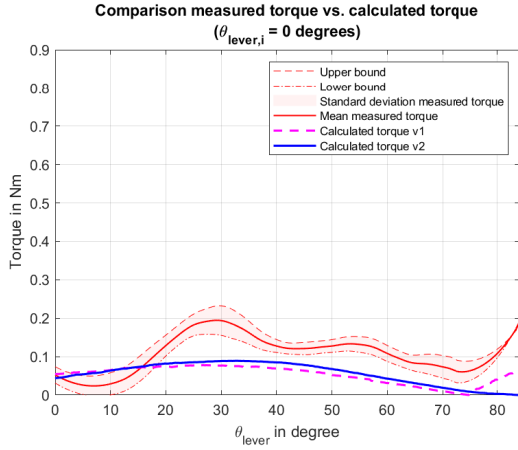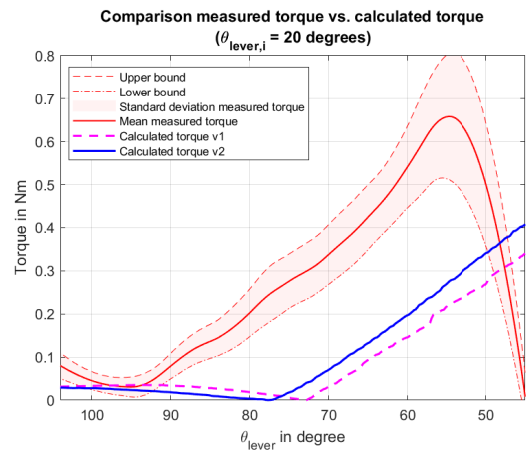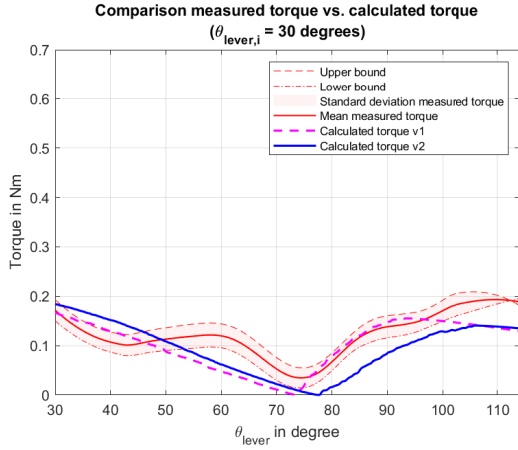
(a) The torque profiles for the folding movement of the parallelogram linkage, meaning that its internal angle (γ_{plg}) increases. The starting angle of the lever arm is $\theta_{lever,i} = 0°$.
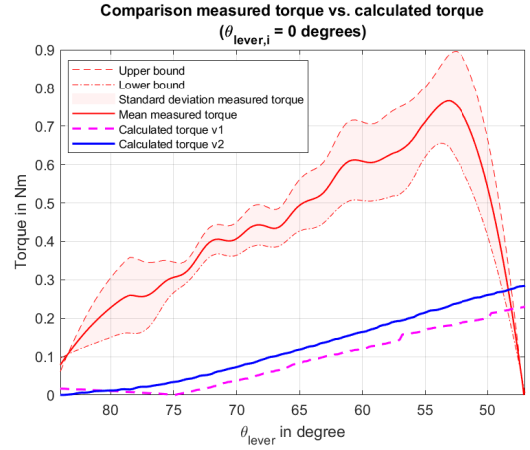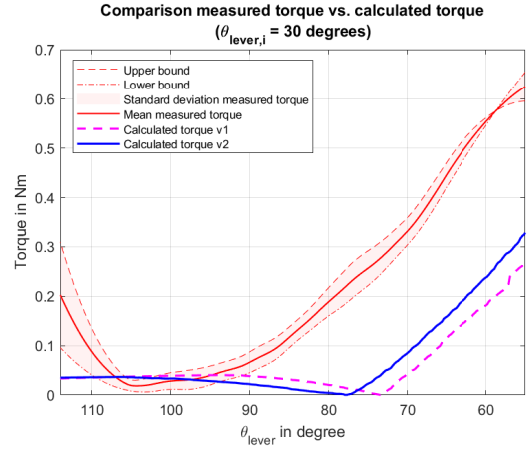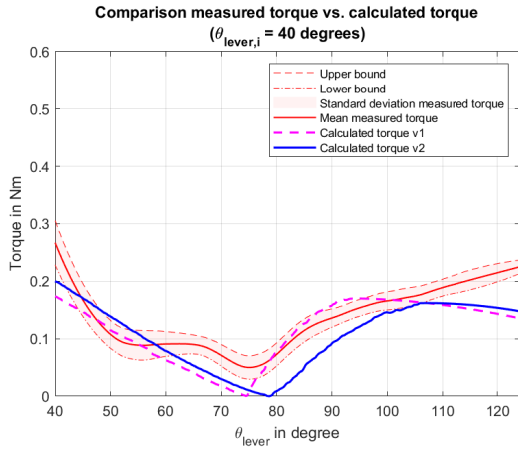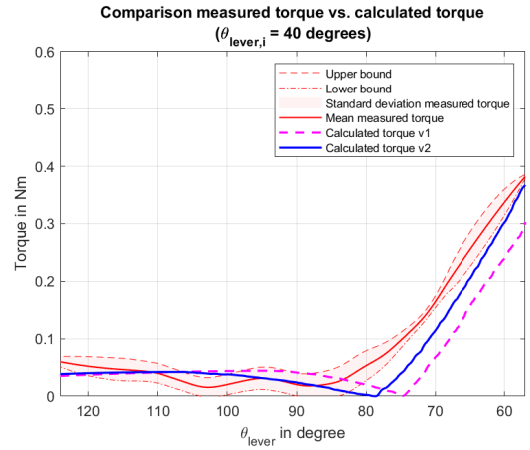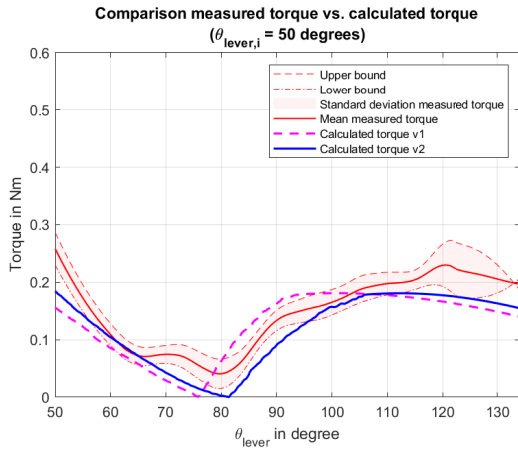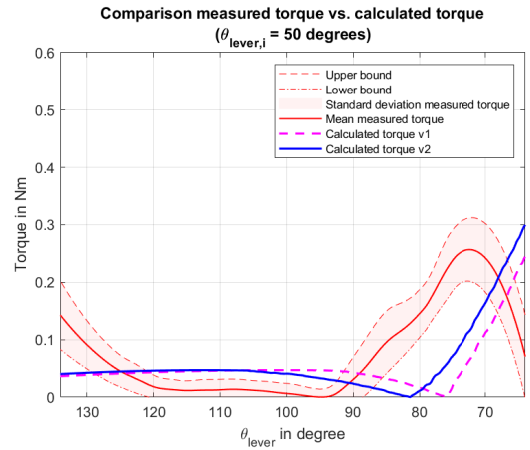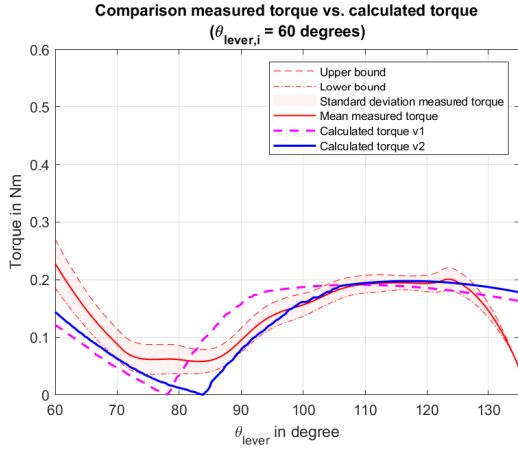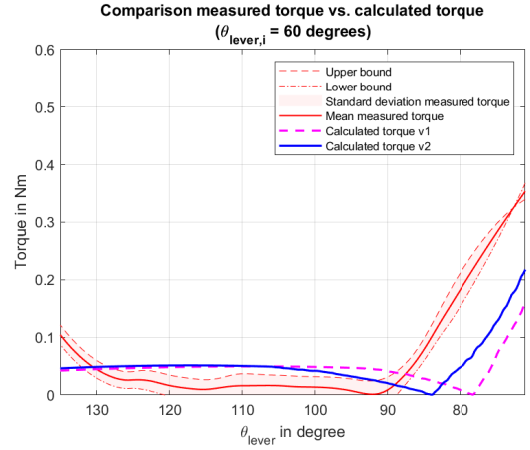
(b) The torque profiles for the opening movement of the parallelogram linkage, meaning that its internal angle (γ_{plg}) decreases. The starting angle of the lever arm is $\theta_{lever,i} = 85°$.
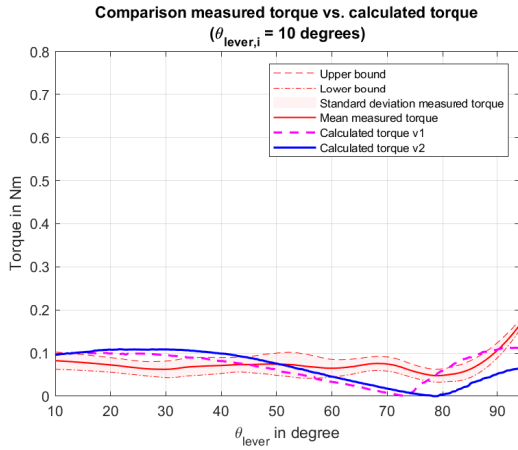
(c) The torque profiles for the folding movement of the parallelogram linkage, meaning that its internal angle (γ_{plg}) increases. The starting angle of the lever arm is $\theta_{lever,i} = 10°$.
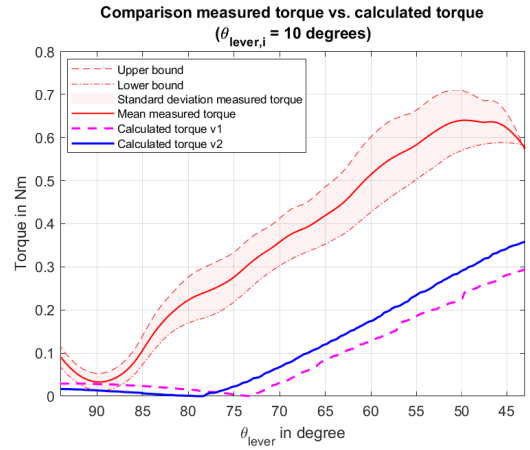
(d) The torque profiles for the opening movement of the parallelogram linkage, meaning that its internal angle (γ_{plg}) decreases. The starting angle of the lever arm is $\theta_{lever,i} = 95°$.
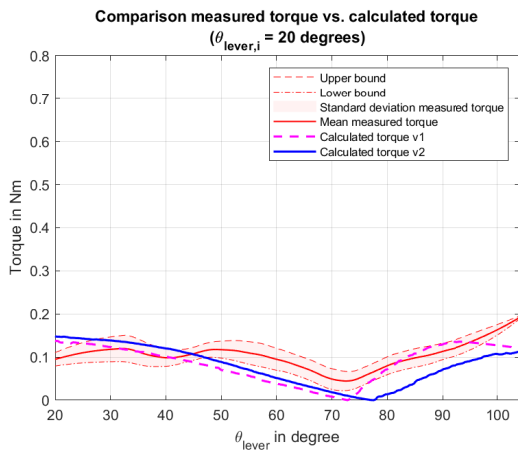
(e) The torque profiles for the folding movement of the parallelogram linkage, meaning that its internal angle (γ_{plg}) increases. The starting angle of the lever arm is $\theta_{lever,i} = 20°$.

(f) The torque profiles for the opening movement of the parallelogram linkage, meaning that its internal angle (γ_{plg}) decreases. The starting angle of the lever arm is $\theta_{lever,i} = 105°$.
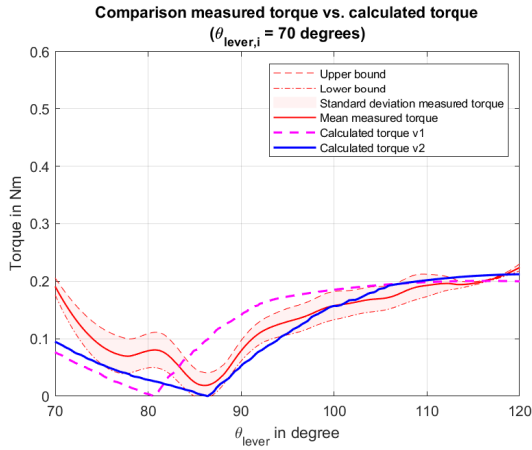
Figure 18: Torque behaviour of the lead screw for folding and opening the parallelogram mechanism with starting angles of the lever arm of $\theta_{lever,i} = 0°, 10°, 20°$. The filtered measured data, represented by a mean (red solid line) and its standard deviation (red shaded region), the calculated torque from the model based on the Skelex 360-XFR (magenta dashed line), and the calculated torque from the model based on prototype I (blue solid line) have been represented. Above each figure, a title has been presented which states that both the folding and opening movement had the same starting angle. The reason for that is, although both plots are shown separately, they are both part of the same trial with the same starting angle of the lever arm ($\theta_{lever,i}$).
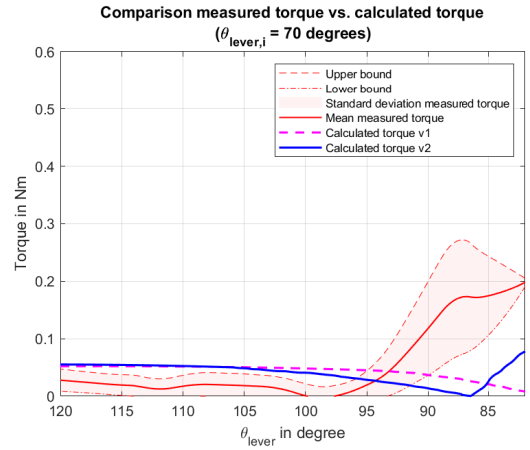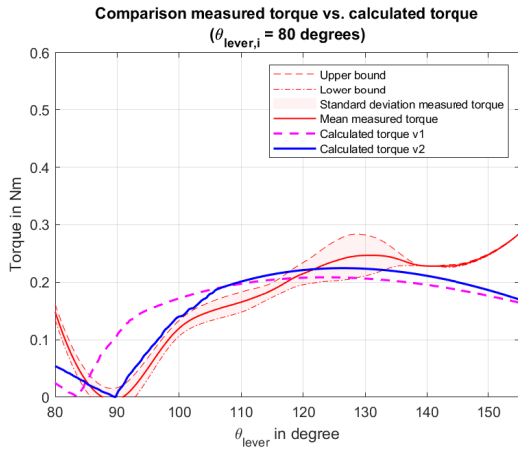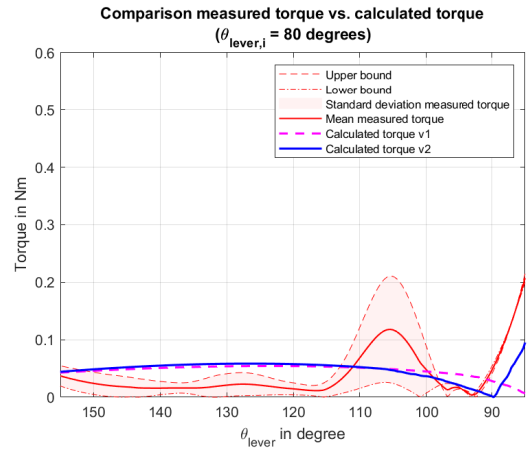
(a) The torque profiles for the folding movement of the parallelogram linkage, meaning that its internal angle (γ_{plg}) increases. The starting angle of the lever arm is $\theta_{lever,i} = 30°$.

(b) The torque profiles for the opening movement of the parallelogram linkage, meaning that its internal angle (γ_{plg}) decreases. The starting angle of the lever arm is $\theta_{lever,i} = 115°$.

(c) The torque profiles for the folding movement of the parallelogram linkage, meaning that its internal angle (γ_{plg}) increases. The starting angle of the lever arm is $\theta_{lever,i} = 40°$.

(d) The torque profiles for the opening movement of the parallelogram linkage, meaning that its internal angle (γ_{plg}) decreases. The starting angle of the lever arm is $\theta_{lever,i} = 125°$.

(e) The torque profiles for the folding movement of the parallelogram linkage, meaning that its internal angle (γ_{plg}) increases. The starting angle of the lever arm is $\theta_{lever,i} = 50°$.

(f) The torque profiles for the opening movement of the parallelogram linkage, meaning that its internal angle (γ_{plg}) decreases. The starting angle of the lever arm is $\theta_{lever,i} = 135°$.

Figure 19: Torque behaviour of the lead screw for folding and opening the parallelogram mechanism with starting angles of the lever arm of $\theta_{lever,i} = 30°, 40°, 50°$. The filtered measured data, represented by a mean (red solid line) and its standard deviation (red shaded region), the calculated torque from the model based on the Skelex 360-XFR (magenta dashed line), and the calculated torque from the model based on prototype I (blue solid line) have been represented. Above each figure, a title has been presented which states that both the folding and opening movement had the same starting angle. The reason for that is, although both plots are shown separately, they are both part of the same trial with the same starting angle of the lever arm ($\theta_{lever,i}$).

(a) The torque profiles for the folding movement of the parallelogram linkage, meaning that its internal angle (γ_{plg}) increases. The starting angle of the lever arm is $\theta_{lever,i} = 60°$.

(b) The torque profiles for the opening movement of the parallelogram linkage, meaning that its internal angle (γ_{plg}) decreases. The starting angle of the lever arm is $\theta_{lever,i} = 135°$.

(c) The torque profiles for the folding movement of the parallelogram linkage, meaning that its internal angle (γ_{plg}) increases. The starting angle of the lever arm is $\theta_{lever,i} = 70°$.

(d) The torque profiles for the opening movement of the parallelogram linkage, meaning that its internal angle (γ_{plg}) decreases. The starting angle of the lever arm is $\theta_{lever,i} = 120°$.

(e) The torque profiles for the folding movement of the parallelogram linkage, meaning that its internal angle (γ_{plg}) increases. The starting angle of the lever arm is $\theta_{lever,i} = 80°$.

(f) The torque profiles for the opening movement of the parallelogram linkage, meaning that its internal angle (γ_{plg}) decreases. The starting angle of the lever arm is $\theta_{lever,i} = 160°$.

Figure 20: Torque behaviour of the lead screw for folding and opening the parallelogram mechanism with starting angles of the lever arm of $\theta_{lever,i} = 60°, 70°, 80°$. The filtered measured data, represented by a mean (red solid line) and its standard deviation (red shaded region), the calculated torque from the model based on the Skelex 360-XFR (magenta dashed line), and the calculated torque from the model based on prototype I (blue solid line) have been represented. Above each figure, a title has been presented which states that both the folding and opening movement had the same starting angle. The reason for that is, although both plots are shown separately, they are both part of the same trial with the same starting angle of the lever arm ($\theta_{lever,i}$).

APPENDIX E
CABLE TENSION COMPARISON PROTOTYPE I VERSUS SKELEX 360-XFR
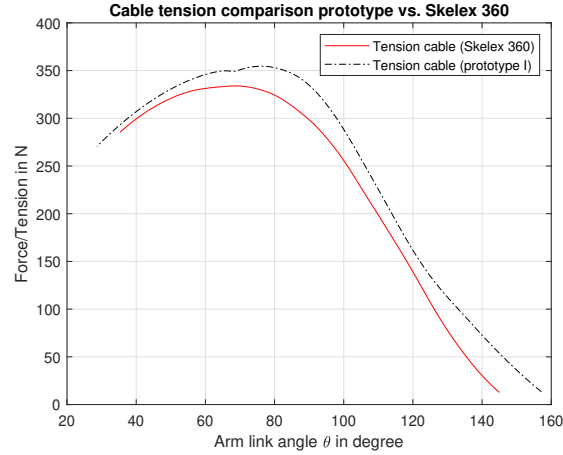
Figure 21: Cable tension comparison between the conventional Skelex 360-XFR exoskeleton and the first prototype (see Figure 17)

APPENDIX F
DERIVATION OF THE BALANCING CONDITIONS BASED ON POTENTIAL ENERGY EQUATIONS

One way of deriving the stiffness of the spring such that it balances out the reaction forces on the lead screw (being induced by the leaf spring and the user's arms) is by using the principle of static balance. When the leaf spring is inducing a resultant force on the lever arm, the parallelogram mechanism tends to fold and is therefore inducing a resultant force on the lead screw. If the total resultant force exerted on the lead screw would be zero, the system must find itself in static balance. In order to achieve that, the purpose of the balancing spring would be to counteract the folding behaviour induced by the leaf spring by inducing a force that tends to open the parallelogram linkage. According to Herder et al. [4], a statically balanced mechanism may be defined as: *"A mechanism on which the forces of one or more potential energy storage elements are acting, such that the mechanism is in static equilibrium, or approximately so, throughout or at least in considerable part of its range of motion, rather than in a single point or a limited number of points only, even in the absence of friction."*

So, in order for the lead screw to be adjusted with almost zero effort, the parallelogram mechanism must find itself in static balance for every possible configuration it can reach. To find out for what stiffness this behaviour can be achieved, the following steps have been taken →

Firstly, we must convert all external forces into forces that are represented by either a gravitational component or a spring force, as we must be able to describe every reaction force in terms of a potential energy equation. An external force can be converted into a gravitational component and into a component running parallel with the link it is acting on. This has also been presented in Figure 22, where the perpendicular component of the user's arm's reaction force and of the cable tension have been converted into a gravitational component and a component running parallel with the link. In this way, the external forces have been converted into gravitational components that can be used in the potential energy equations. It has to be mentioned that this only holds true in the case where the lever arm keeps its configuration and does not rotate. A rotation of the lever arm would imply a different cable tension, and thus also a different gravitational component at both the arm- and lever arm link. The same applies for a rotation of the arm link, because during rotation of it the vertical (or gravitational) component is varying. Therefore, the assumption has been made for now that both links keep their position. Just as discussed in Herder et al. [10], [4], a zero free length spring has been integrated in this concept where the spring force is proportional to its length. Utilizing all the above-mentioned conversions, leads to the following principles for static balance of the parallelogram →

$$V_{m1} = m_1 \cdot d_{arm} \cdot \cos(\gamma_{plg}) \tag{13}$$

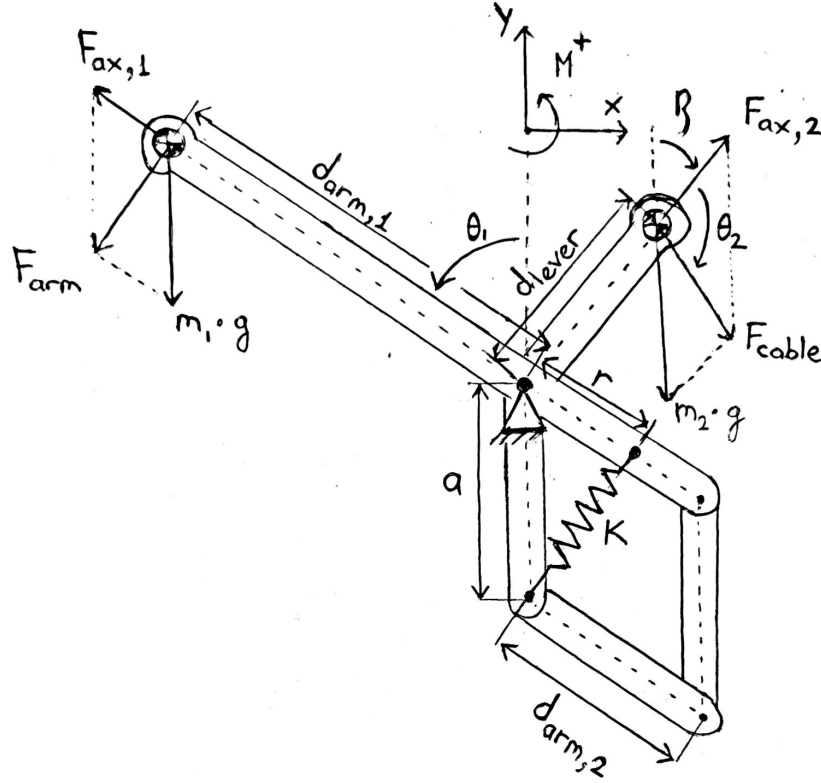$$V_{m2} = m_2 \cdot d_{lever} \cdot \cos(\beta) \tag{14}$$

Figure 22: The drawing of the parallelogram linkage in a configuration such that potential energy equations can be used to derive the conditions for static balance, as explained by Herder et al. [10]. In the figure, both the cable force F_{cable} and the arm's reaction force F_{arm} have been decomposed in a gravitational and axial component. The other parameters refer to the following: θ_1 the angle of the arm link w.r.t. the y-axis, β the angle of the lever arm w.r.t. the y-axis, θ_2 the angle of the cable w.r.t. lever arm link, $d_{arm,1}$ the length of the arm link, $d_{arm,2}$ the length of the other side of the arm link, 'a' the distance from the fixed end of the spring to the main pivot, 'r' the distance from the moving end of the spring to the main pivot, and 'k' the stiffness of the zero-free-length spring.

$$V_{sp} = 0.5 \cdot k \cdot (a^2 + r^2) - k \cdot a \cdot r \cdot \cos(\gamma_{plg}) \tag{15}$$

Combining the potential energy equations presented above, gives the total potential energy equation of the parallelogram mechanism:

$$V_{total} = V_{m1} + V_{m2} + V_{sp} \tag{16}$$

As it is desired to have static balance in the parallelogram mechanism, such that very little effort is needed to adjust its configuration, we must use the fact that for static balance the total potential energy in the system must be 0 for every internal angle (γ_{plg}) of the parallelogram. This yields the following equation for a static balance $\rightarrow$

$$\frac{dV_{total}}{d\gamma_{plg}} = 0 \rightarrow m_1 \cdot g \cdot d_{arm} \cdot \sin(\gamma_{plg}) = k \cdot a \cdot r \cdot \sin(\gamma_{plg}) \tag{17}$$

Solving Equation 17 for the spring stiffness brings us to the following $\rightarrow$

$$k = \frac{m_1 \cdot g \cdot d_{arm}}{a \cdot r} \tag{18}$$

As mentioned before, we converted the reaction force of the user's arms acting on the arm cup into a vertical component representing the gravitational component, and a component running parallel with the link in order to be able to make use of the potential energy equations. As it is desired to express the stiffness in terms of the (known) cable tension F_{cable}, the gravitational component $m_1 \cdot g$ needs to be expressed in terms of F_{cable} and substituted back in the formula of the stiffness (Equation 18). m_1 can be computed in terms of F_{cable} by imagining the whole mechanism to act as one rigid body and using the fact that for equilibrium, the sum of moments across the main hinge 'R' must be zero $\rightarrow$

$$\sum M_R = 0 \rightarrow m_1 = \frac{F_{cable} \cdot \sin(\theta_{cable}) \cdot d_{lever}}{g \cdot \sin(\gamma_{plg}) \cdot d_{arm}} \tag{19}$$

Substituting Equation 19 back into Equation 18 brings us to the following equation for the balancing spring's stiffness for a static balance of the mechanism →

$$k = \frac{F_{cable} \cdot \sin(\theta_{cable}) \cdot d_{lever}}{\sin(\gamma_{plg}) \cdot a \cdot r} \tag{20}$$

As observable from Equation 20 static balance of the parallelogram linkage can only be achieved if both θ_{cable} and γ_{plg} would remain constant. This is the simplification that has been made and, thus, shows that when parameters a, r and d_{lever} remain constant, static balance can never be achieved for multiple configurations of the mechanism. Though, theoretically, it could be possible to reach a static balance in the parallelogram for every possible configuration if, for instance, d_{lever} would be a function of $\sin(\gamma_{plg})$ and a or r would be a function of $\sin(\theta_{cable})$.
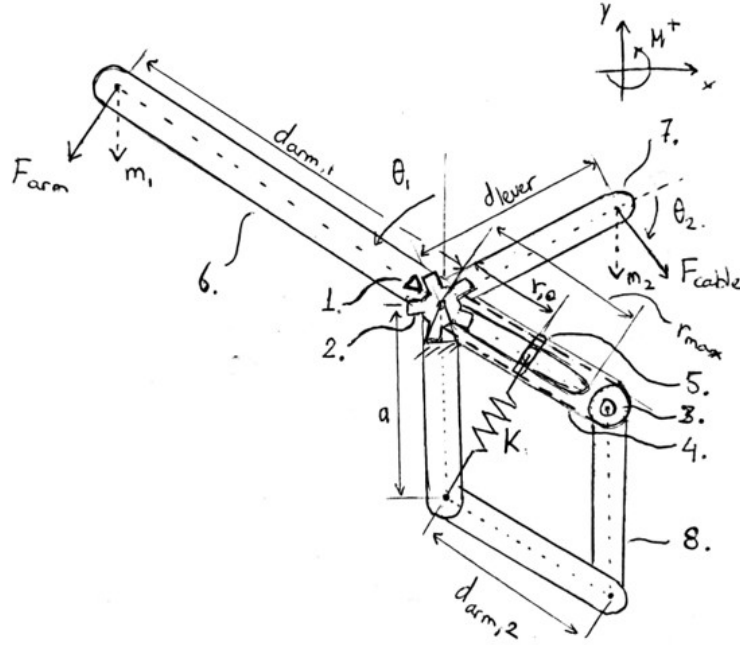
Figure 23: Drawing of the concept in which static balance could be preserved during a rotation of the arm link, under the assumption that the position of the lever arm with respect to the y-axis remains equal. The labels in the figure refer to the following: 1. a pin interfering with the gear, 2. the gear, 3. a guiding pulley, 4. a timing belt connected to the gear and the guiding pulley, 5. a slider, 6. the arm link, 7. the lever arm link, 8. the coupler link.

A possible concept where this behaviour could be achieved has been presented in Figure 23. Here, distance r has become a function of γ_{plg}, such that both could theoretically cancel each other out (in Equation 18) if r would follow a path dependent on the inverse sine of γ_{plg}. The concept as presented in Figure 23 works as follows:

When the arm link (6.) rotates, such that γ_{plg} becomes larger, pin (1.) transmits this rotation to a gear (2.) over which a cable (4.) runs that is attached to a slider (5.) and guided by a pulley (3.) such that it functions as a closed loop mechanism. This means that if the arm link rotates, and thus pin (1.) rotates the gear (2.), the distance r will be changed as well. The change in r will be determined by the rotation 1 and the radius of the gear (2.), computed as follows →

$$r_{\gamma_{plg}} = r_{gear} \cdot \gamma_{plg} \tag{21}$$

Using the fact that $r_{\gamma_{plg}}$ must be equal to r as being used in Equation 20, we now have obtained two equations for r that must be equal to each other. Solving this for the radius of the gear gives the following →

$$r_{\gamma_{plg}} = r \rightarrow r_{gear} = \frac{F_{cable} \cdot \sin(\theta_{cable}) \cdot d_{lever}}{k \cdot a \cdot \gamma_{plg}} \tag{22}$$

To analyze whether this could be a feasible solution, a few realistic parameters have been filled in the formula for the gear's radius, as presented in Equation 22. Using the known domain for θ_{cable} running from approximately 0 to 120 degrees in the Skelex 360-XFR, the maximum lever arm length of 50 mm, and the known cable tension belonging to each value of θ_{cable}, we have obtained a plot (see Figure 24) that shows what the radius of the gear must be in order to make the stiffness independent on the internal angle of the parallelogram (γ_{plg}).
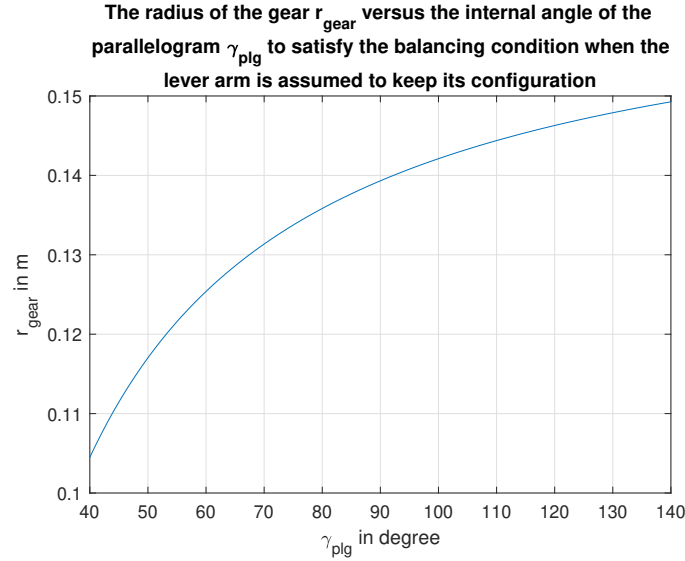
Figure 24: Radius of the conceptual gear, belonging to a change in internal angle of the parallelogram. Note that this shape has been derived under the assumption that the lever arm link keeps its configuration, and thus only the arm link rotates.

Figure 24 shows that the radius of the gear must lie within the range of 0.1-0.2 [m]. This is regarded as being too large to be implemented in the parallelogram, as important requirements are related to the dimensions of the design. Furthermore, a lot of assumptions have been made that in reality are not necessarily always valid. For instance, the lever arm will not always keep its configuration. In most of the cases, the lever arm will rotate during usage, making it necessary to also cancel out the dependency of the static balance on θ_{cable}. This, again, takes up space which is very scarce in this mechanism.

Another downside of this concept is that when the attachment points of the spring in the parallelogram are being passively replaced during rotation of the arm link for instance, this will induce extra forces which may interfere with the desired sine shaped force-angle curve the Skelex 360-XFR is providing to the user. Overall, it can be stated that this is an unfeasible solution to this design problem.

APPENDIX G
LABVIEW BLOCK SCHEME
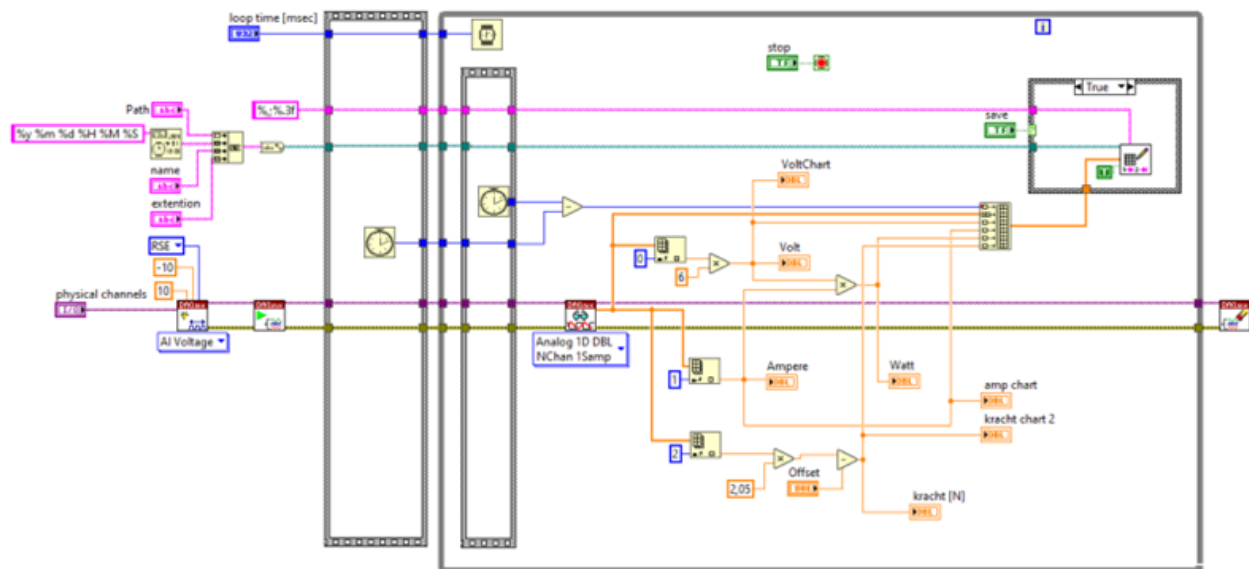
Figure 25: Block scheme for the storage of the motor's current consumption as being created by J. van Driel from the TU Delft Meetshop. In total a number of 8 outputs are given by the scheme, of which only the current consumption, voltage across the motor, and the time are of interest.

APPENDIX H
TORQUE-CURRENT CONSTANT EXPERIMENT

(a)   (b)
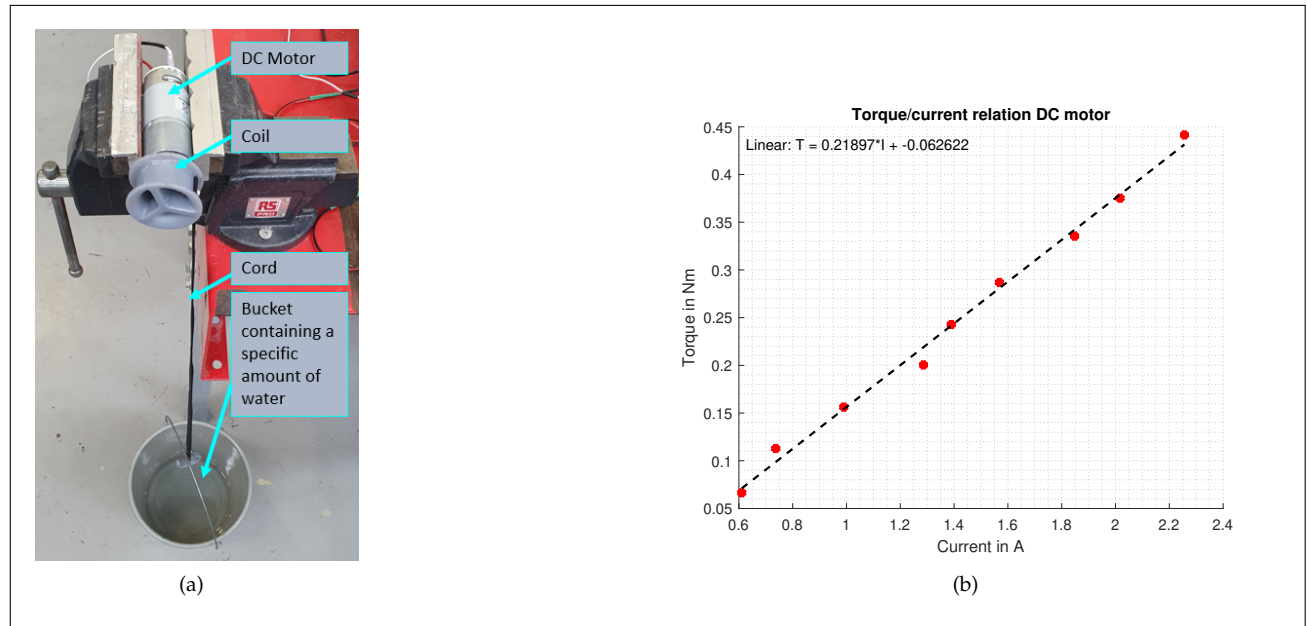
Figure 26: Visual representation of the experiment in which the current-torque relation of the DC-motor has been derived. **(a)** The experimental set-up for the derivation of the torque-current constant of the DC-motor being used in the main validation experiment. Each component has been indicated by an arrow and a text box. The power and data acquisition systems have not been depicted, but are part of the experiment. **(b)** The visual presentation of the derivation of the torque-current relationship of the DC-motor. A linear fit could be made through the data points which belong to specific known weights and the current consumption as a result of those weights. The exact relation has been indicated in the left top in the form of y=Ax+b.

APPENDIX I
SPECIFICATIONS OF THE LEAD SCREW NUT

Algemene eigenschappen	
Materiaal	iglidur® J
Schroefdraadrichting	Rechtse schroefdraad
Draadtype	Trapezoïdale schroefdraad
Gewicht	7,02 g
Dichtheid	1,49 g/cm^3
Kleur	geel
Max. vochtabsorptie (bij 23 °C/73 °F, 50% r.v.)	0,3 gew.-%, testmethode DIN 53495
Max. water absorptie	1,3 gewichtsprocent
Coëfficient van glijwrijving, dynamisch, op staal	0,06 - 0,18 µ
pv-waarde, max. (droog)	0,34 MPa · m/s

Afmetingen	
Draad	Tr10X3
Ø d1	10,00 mm
Ø d2	20,0 mm
b1	20,00 mm
Doelmatig steunoppervlak	267 mm²
A□	18,00 mm

Mechanische eigenschappen	
Elasticiteitsmodus	2.400 MPa, testmethode DIN 53457
Buigsterkte (bij 20 °C/68 °F)	73 MPa, testmethode DIN 53452
Drukbelasting	60 MPa
Max. aanbevolen oppervlaktedruk (bij +20 °C/68 °F)	35 MPa
Shore-D hardheid	74, testmethode DIN 53505

Figure 27: The specifications of the lead screw nut as supplied by the manufacturer (IGUS).

APPENDIX J
MODEL VALIDATION CODE

For the MATLAB script, see MATLAB code Model Validation.

APPENDIX K
WORKING PRINCIPLE CODE

For the MATLAB script, see MATLAB code Working Principle Validation.

APPENDIX L
ZERO-LOAD MEASUREMENT DC MOTOR
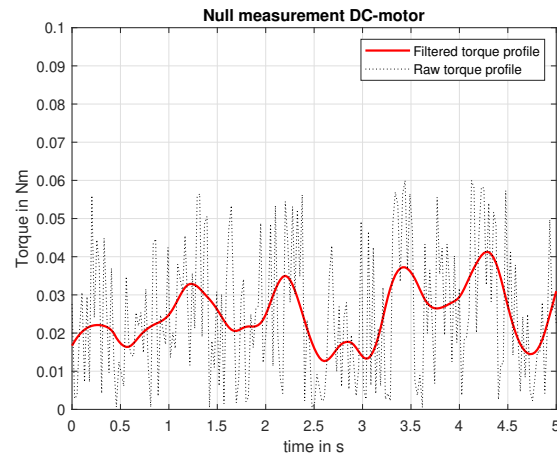
Figure 28: Zero-load measurement of the DC-motor utilized in the final prototype. Both the raw data and the filtered data have been presented, to show the periodicity of the current consumption (and thus torque output).

APPENDIX M
UNFILTERED RESULTS MODEL VALIDATION EXPERIMENT
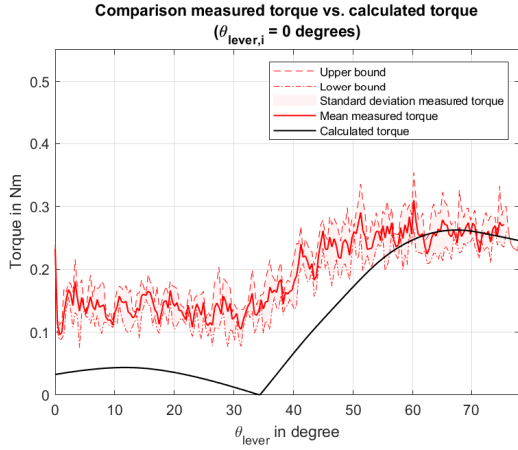
(a) The torque profiles for the folding movement of the parallelogram linkage, meaning that its internal angle (γ_{plg}) increases. The starting angle of the lever arm is $\theta_{lever,i} = 0°$.
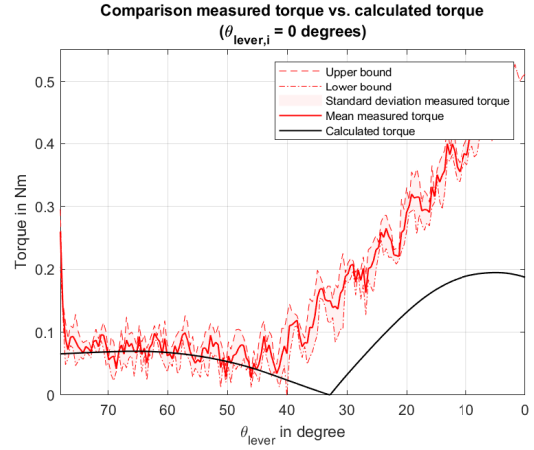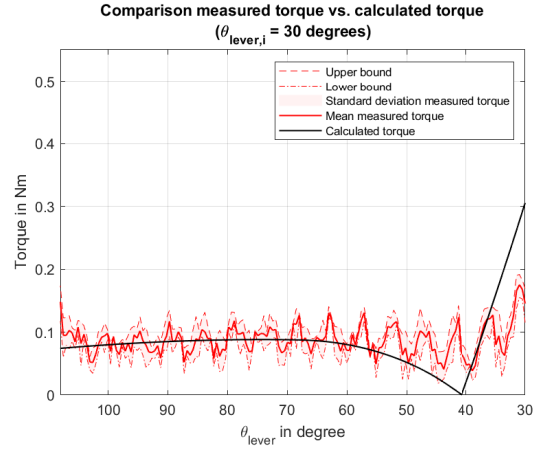
(b) The torque profiles for the opening movement of the parallelogram linkage, meaning that its internal angle (γ_{plg}) decreases. The starting angle of the lever arm is $\theta_{lever,i} = 80°$.
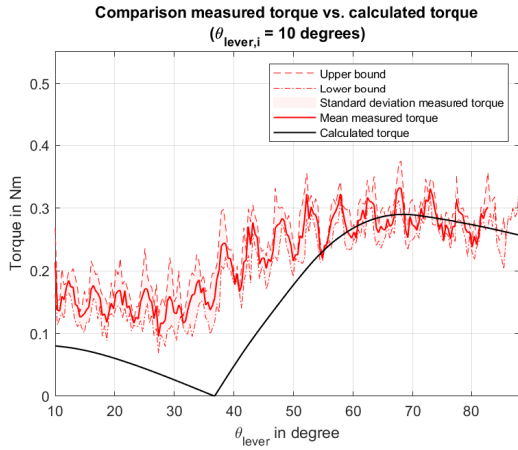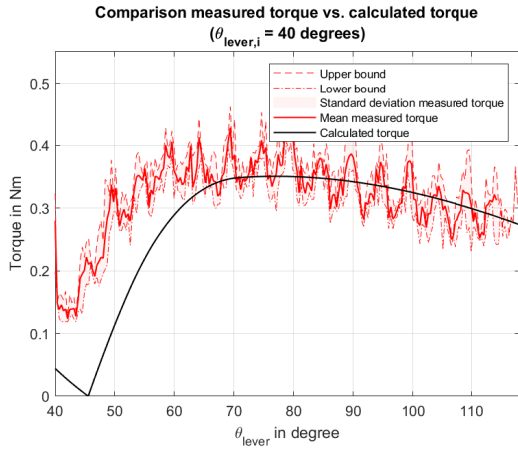
(c) The torque profiles for the folding movement of the parallelogram linkage, meaning that its internal angle (γ_{plg}) increases. The starting angle of the lever arm is $\theta_{lever,i} = 10°$.
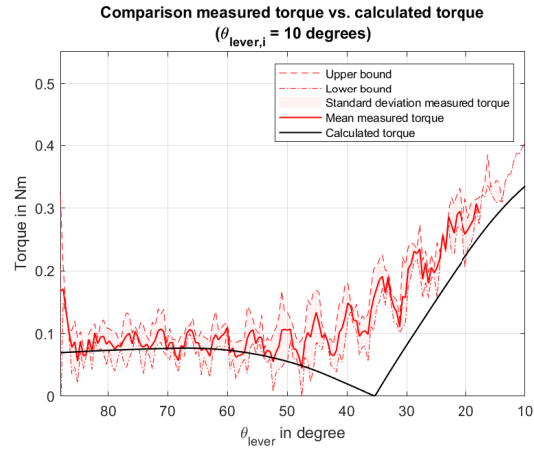
(d) The torque profiles for the opening movement of the parallelogram linkage, meaning that its internal angle (γ_{plg}) decreases. The starting angle of the lever arm is $\theta_{lever,i} = 90°$.
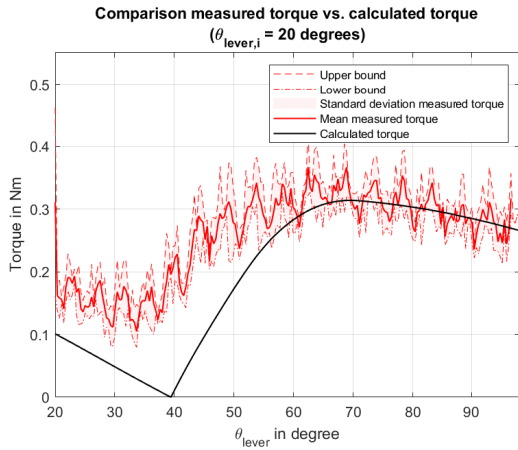
(e) The torque profiles for the folding movement of the parallelogram linkage, meaning that its internal angle (γ_{plg}) increases. The starting angle of the lever arm is $\theta_{lever,i} = 20°$.
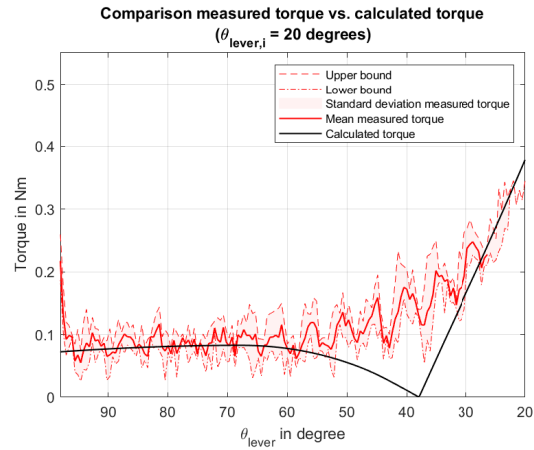
(f) The torque profiles for the opening movement of the parallelogram linkage, meaning that its internal angle (γ_{plg}) decreases. The starting angle of the lever arm is $\theta_{lever,i} = 100°$.

Figure 29: Torque behaviour of the lead screw for folding and opening the parallelogram mechanism with starting angles of the lever arm of $\theta_{lever,i} = 0°, 10°, 20°$. Both the raw measured data, represented by a mean (red solid line) and its standard deviation (red shaded region), and the calculated torque from the model (black solid line) have been represented. Above each figure, a title has been presented which states that both the folding and opening movement had the same starting angle. The reason for that is, although both plots are shown separately, they are both part of the same trial with the same starting angle of the lever arm ($\theta_{lever,i}$).

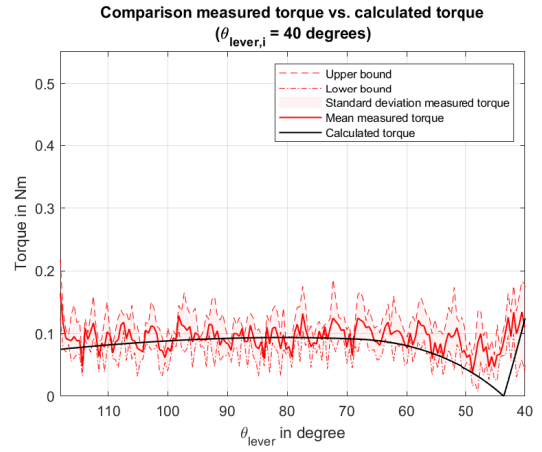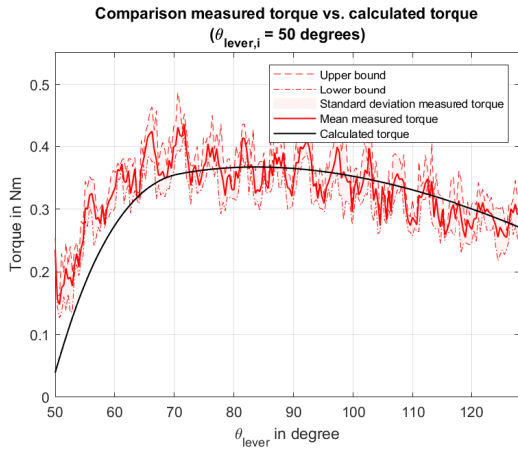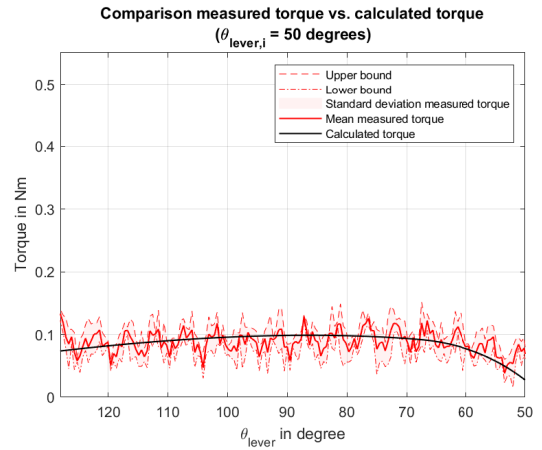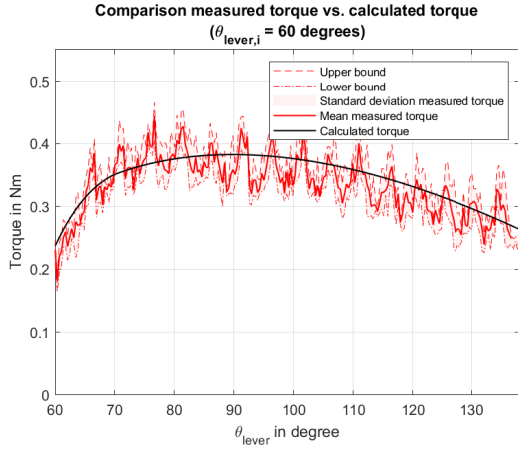(a) The torque profiles for the folding movement of the parallelogram linkage, meaning that its internal angle (γ_{plg}) increases. The starting angle of the lever arm is $\theta_{lever,i} = 30°$.

(b) The torque profiles for the opening movement of the parallelogram linkage, meaning that its internal angle (γ_{plg}) decreases. The starting angle of the lever arm is $\theta_{lever,i} = 110°$.

(c) The torque profiles for the folding movement of the parallelogram linkage, meaning that its internal angle (γ_{plg}) increases. The starting angle of the lever arm is $\theta_{lever,i} = 40°$.
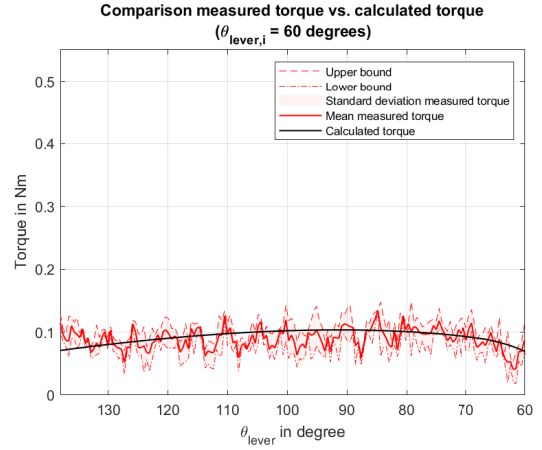
(d) The torque profiles for the opening movement of the parallelogram linkage, meaning that its internal angle (γ_{plg}) decreases. The starting angle of the lever arm is $\theta_{lever,i} = 120°$.

(e) The torque profiles for the folding movement of the parallelogram linkage, meaning that its internal angle (γ_{plg}) increases. The starting angle of the lever arm is $\theta_{lever,i} = 50°$.

(f) The torque profiles for the opening movement of the parallelogram linkage, meaning that its internal angle (γ_{plg}) decreases. The starting angle of the lever arm is $\theta_{lever,i} = 130°$.
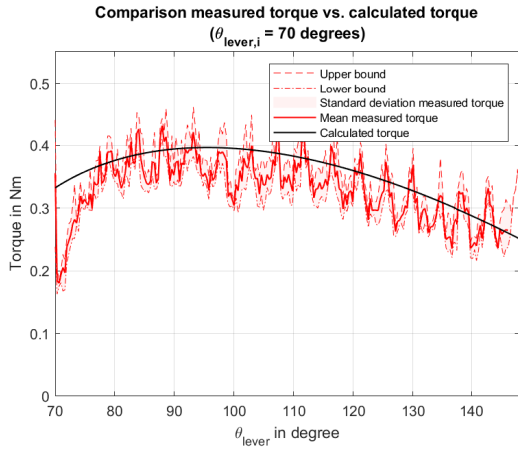
Figure 30: Torque behaviour of the lead screw for folding and opening the parallelogram mechanism with starting angles of the lever arm of $\theta_{lever,i} = 30°, 40°, 50°$. Both the raw measured data, represented by a mean (red solid line) and its standard deviation (red shaded region), and the calculated torque from the model (black solid line) have been represented. Above each figure, a title has been presented which states that both the folding and opening movement had the same starting angle. The reason for that is, although both plots are shown separately, they are both part of the same trial with the same starting angle of the lever arm ($\theta_{lever,i}$).
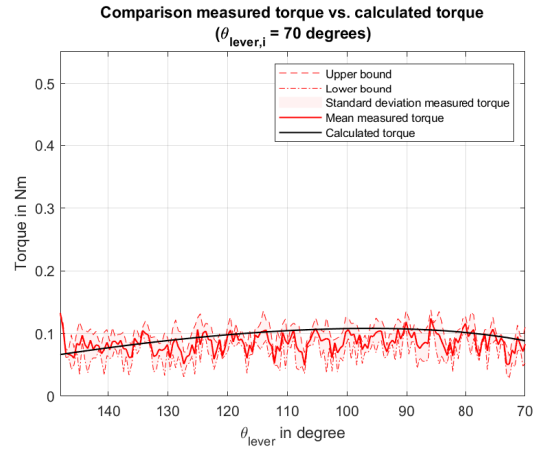
(a) The torque profiles for the folding movement of the parallelogram linkage, meaning that its internal angle (γ_{plg}) increases. The starting angle of the lever arm is $\theta_{lever,i} = 60°$.
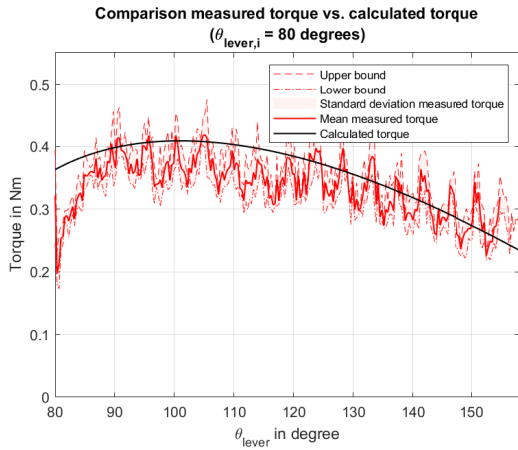
(b) The torque profiles for the opening movement of the parallelogram linkage, meaning that its internal angle (γ_{plg}) decreases. The starting angle of the lever arm is $\theta_{lever,i} = 140°$.
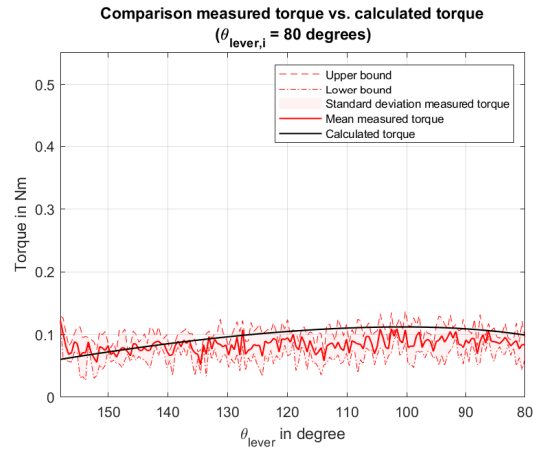
(c) The torque profiles for the folding movement of the parallelogram linkage, meaning that its internal angle (γ_{plg}) increases. The starting angle of the lever arm is $\theta_{lever,i} = 70°$.

(d) The torque profiles for the opening movement of the parallelogram linkage, meaning that its internal angle (γ_{plg}) decreases. The starting angle of the lever arm is $\theta_{lever,i} = 150°$.

(e) The torque profiles for the folding movement of the parallelogram linkage, meaning that its internal angle (γ_{plg}) increases. The starting angle of the lever arm is $\theta_{lever,i} = 80°$.

(f) The torque profiles for the opening movement of the parallelogram linkage, meaning that its internal angle (γ_{plg}) decreases. The starting angle of the lever arm is $\theta_{lever,i} = 160°$.

Figure 31: Torque behaviour of the lead screw for folding and opening the parallelogram mechanism with starting angles of the lever arm of $\theta_{lever,i} = 60°, 70°, 80°$. Both the raw measured data, represented by a mean (red solid line) and its standard deviation (red shaded region), and the calculated torque from the model (black solid line) have been represented. Above each figure, a title has been presented which states that both the folding and opening movement had the same starting angle. The reason for that is, although both plots are shown separately, they are both part of the same trial with the same starting angle of the lever arm ($\theta_{lever,i}$).